System-Conditioned Reparameterization of the SCAN Functional for Accurate Bandgaps: From Analytical Constraints to Machine Learning

Viviana Dovale-Farelo*
Department of Physics, West Virginia University, Morgantown, WV 26506, USA
Material Measurement Laboratory, National Institute of Standards and Technology, Maryland, 20899, USA. and
University of Maryland, College Park, MD, 20742, USA

Pedram Tavadze
Department of Physics, West Virginia University, Morgantown, WV 26506, USA

Miguel A. L. Marques
Research Center Future Energy Materials and Systems of the University Alliance Ruhr, Faculty of Mechanical Engineering, Ruhr University Bochum, Universitätsstraße 150, D-44801 Bochum, Germany

Srinjoy Das
School of Mathematical and Data Sciences, West Virginia University, Morgantown, WV 26506, USA

Kamal Choudhary
Material Measurement Laboratory, National Institute of Standards and Technology, Maryland, 20899, USA.

Alejandro Bautista-Hernández
Facultad de Ingeniería, Benemérita Universidad Autónoma de Puebla, Edificio ING2, Ciudad Universitaria, CP. 72570 Puebla, México

Aldo H. Romero
Department of Physics, West Virginia University, Morgantown, WV 26506, USA and
Facultad de Ingeniería, Benemérita Universidad Autónoma de Puebla, Edificio ING2, Ciudad Universitaria, CP. 72570 Puebla, México

*Corresponding Author: vd0020@mix.wvu.edu
(Dated: April 17, 2026)

Abstract

This work investigates how reparametrizing the Strongly Constrained and Appropriately Normed (SCAN) exchange–correlation (XC) functional within density functional theory affects predictions of the electronic bandgap (E_g) for solids. A system dependent functional (SD-SCAN) is proposed by adjusting a subset of SCAN's internal parameters to improve bandgaps. For most covalent materials, SD-SCAN yields bandgaps closer to experimental values while preserving accurate lattice constants; improvements remain limited for highly ionic systems, reflecting constraints of SCAN's α-dependence and the absence of long-range nonlocal (Hartree–Fock-like) exchange at the semilocal/meta-GGA level. The modified parameters enhance exchange in regions with covalent character, raising the conduction bands and broadening the charge density, thereby yielding more realistic electronic structures and improved dielectric response. A machine-learning model (ML-SCAN) predicts SCAN parameters from solid-state descriptors, providing a flexible, system-dependent reparametrization strategy competitive with existing semilocal approaches. A simplified variant, SCAN-0.2, offers a fixed-parameter shortcut for improved bandgap calculations. Overall, this study lays the groundwork for ML-driven XC functionals for semiconductors.

I. INTRODUCTION

The electronic bandgap (E_g) determines whether a material acts as a conductor, semiconductor, or insulator. Semiconductors have a moderate E_g, allowing controlled electron flow [1]. This makes these materials special because their switching behavior (conducting and non-conducting) underpins electronic devices such as switches and transistors, driving the current electronic era [2]. Semiconductors also interact with light, absorbing or emitting photons at specific wavelengths, thereby enabling optoelectronic devices such as LEDs, lasers, and solar cells [3]. Some semiconductors display thermoelectric properties, converting heat energy into electrical energy through the Seebeck effect [4]. Advancing the understanding of semiconductors is key to furthering semiconductor technology and unlocking the next wave of technological innovation.

Unfortunately, reliably predicting the band gap (E_g) of

semiconductors and insulators remains challenging due to the many-body nature of the Schrödinger equation in quantum mechanics. Solids pose a high-dimensional problem, with calculations scaling to 3N dimensions, where N is the number of electrons. Density Functional Theory (DFT) simplifies this by reducing the dimensionality from 3N to 3, using the electron density as the central variable. However, DFT has limitations. The exact exchange-correlation (XC) functional, which describes all quantum mechanical interactions between electrons, remains unknown [5, 6]. While current approximations have achieved notable success in improving bandgap predictions, challenges persist in achieving consistent accuracy across a broad range of materials, particularly for systems requiring a delicate balance between computational cost and precision.

Increasing accuracy demands greater computational resources as one ascends the hierarchy of XC functionals in DFT. The simplest XC functional, Local Density Approximation (LDA), uses only the electron density $n(\mathbf{r})$ [7–9]. The Generalized Gradient Approximation (GGA) includes the gradient of the electron density $\nabla n(\mathbf{r})$ in its formulation [10]. Meta-GGAs, such as the Strongly Constrained and Appropriately Normed (SCAN) functional [11], incorporate the kinetic energy density, $\tau(\mathbf{r})$, to improve accuracy.

Beyond semilocal approximations, hybrid functionals, such as the Heyd–Scuseria–Ernzerhof (HSE) functional [12–15], improve the accuracy of electronic structure predictions by incorporating a fraction of Hartree-Fock exchange. Many-body methods, such as the GW approximation [16–19], provide a more rigorous treatment of electron correlation through quasiparticle self-energy corrections. These corrections account for dynamic electron-electron interactions that are not captured by standard DFT, yielding more reliable bandgap predictions. While both approaches offer high accuracy, they are computationally demanding, which limits their applicability to large or complex systems.

Within the framework of local and semilocal functionals (e.g., LDA and GGA), XC functionals struggle with strong electron-electron correlation in highly correlated materials (d- and f-electrons), electronic bandgap accuracy, precise magnetic ordering, and weak van der Waals interactions [5, 20]. However, significant progress has been made in describing van der Waals interactions, including optB88vdW for dispersion- and hydrogen-bonded systems at the GGA level [21], SCAN+rVV10 for integrating meta-GGA with non-local correlations [22], and SCAN+D3 for incorporating London dispersion corrections to improve the accuracy of molecular and crystal properties [23].

Bandgap underestimation in standard Kohn-Sham (KS) DFT, often by as much as 50% compared to experimental values, primarily arises from limitations in the XC functional.

The KS eigenvalue gap generally differs from the fundamental (quasiparticle) gap because the latter contains the XC derivative discontinuity. While the fundamental gap is defined through total-energy differences, the KS gap is obtained from single-particle eigenvalues and therefore lacks this discontinuous XC contribution. As a result, approximate KS functionals systematically underestimate bandgaps. [6, 24]. By contrast, in the generalized Kohn–Sham (GKS) framework, meta-GGAs and hybrid functionals employ nonlocal potentials that can reproduce accurate gaps via a discontinuity-like response of the effective potential [25–27]. However, some studies show that accurate bandgaps can be obtained without an explicit jump: within GKS, meta-GGAs, and hybrids improve predictions by better capturing the XC potential [28, 29].

Another contributing factor is the incomplete removal of self-interaction in approximate DFT. Unlike Hartree–Fock, which cancels self-interaction exactly, most semilocal XC approximations leave residual self-interaction, shifting the energies of occupied and unoccupied states and narrowing the predicted gap.

Additionally, semilocal KS potentials lack long-range nonlocal (Hartree–Fock-like) exchange, which is essential for accurately describing charge-separated and highly ionic systems; this nonlocal component is partly recovered in GKS hybrids through the inclusion of exact exchange, which opens the bandgap.

Finally, while standard XC functionals include electron–electron interactions approximately, they do not explicitly account for quasiparticle self-energy corrections and electron–hole (excitonic) interactions, which are also crucial for realistic bandgap estimation [6]. Methods like GW and the Bethe–Salpeter Equation address these limitations by including quasiparticle and excitonic effects beyond conventional DFT [30].

Functionals such as the modified Becke-Johnson potential (mBJ) [31], the Thilo Aschebrock and Stephan Kümmel (TASK) functional [32], and machine learning (ML) approaches [33] have significantly improved predictions of E_g. As shown in Supplementary Table 1, the SCAN meta-GGA reduces the average relative error in E_g compared to PBE [10].

SCAN was constructed via a constraint-guided, nonempirical strategy aimed at improving reliability and transferability across diverse bonding environments; its improved performance for self-interaction and certain correlated cases is a consequence of this design rather than its primary target.

In contrast, mBJ and TASK were specifically developed to improve bandgap predictions and generally outperform SCAN in this regard. However, mBJ is unsuitable for structural relaxation, and TASK shows variability in predicting other properties [34]. Recently, the nonempirical Lebeda-Aschebrock-Kümmel (LAK) meta-GGA was introduced, which improves bond energies and bandgaps by rebalancing the density-gradient and kinetic-energy-density contributions in the second-order gradient expansion of the XC energy [35, 36].

Supplementary Table 1 shows that the GW functional

(one-shot G_0W_0@PBE) performs well for most solids, outperforming hybrids for noble gases and wide-bandgap insulators (e.g., LiCl, LiF) due to its accurate treatment of electron-electron interactions [19]. Hybrid functionals also improved bandgap predictions and reliably described semiconductors and heavy-element systems [37–39]. Both GW and hybrids outperformed SCAN and matched mBJ and TASK in specific cases, but at a higher computational cost.

This underscores that, despite more than 500 XC functionals [40, 41], computationally efficient and accurate bandgap prediction, while balancing other material properties, remains challenging.

Several studies have applied ML techniques in conjunction with DFT to predict the bandgaps of solids. For instance, in 2020, Lentz et al. [42] used ML to predict hybrid functional bandgaps from PBE-derived charge densities, and despite a small dataset of seven materials, simulations with various dopants and temperatures expanded the training set, offering HSE-level accuracy at GGA-level cost. In 2024, Liu et al. [43] performed a high-throughput study using structural, compositional, and PBE bandgap features to predict HSE bandgaps. Although experimental data were not used for training, they served as a benchmark for evaluating the predictions. Also, in 2020, Borlido et al. [33] combined structural and compositional features with outputs from multiple XC functionals to predict experimental bandgaps. Their model improved accuracy in the 0.9–2 eV range, although performance declined outside this range. They also reparametrized XC functionals to reduce errors, sometimes overestimating small bandgaps. Later, Pokharel et al. [44] trained ML models to mimic SCAN by predicting XC enhancement factors using the Laplacian of electron density instead of kinetic energy density. The focus was not on bandgaps but on XC energies, atomization energies, and lattice constants—showing promising results for atoms and molecules, but limited transferability to solids. Similarly, Nagai et al. [45] developed a ML-based XC functional trained on molecular data, using local density, gradients, and kinetic energy density. The model optimized XC enhancement factors against properties such as atomization energies, ionization potentials, and electron densities—but did not include bandgap prediction. More recently, Bystrom and Kozinsky developed a nonlocal, orbital-dependent ML exchange functional that obeys exact constraints and can be evaluated at (roughly) semilocal cost, achieving hybrid-like accuracy for molecules and solids and improving bandgap predictions over standard meta-GGAs [46]. These studies highlight the expanding potential of integrating ML with DFT to enhance both the accuracy and efficiency of bandgap predictions.

This work examines whether accurate bandgap prediction can be achieved through system-specific adjustment of XC functional parameters, thereby enabling the semilocal SCAN functional to reflect better the bonding environment and electronic structure of each material. The SCAN functional and its governing parameters are described to test this hypothesis. A selection of 20 representative semiconductors and insulators is analyzed by exploring the 7-dimensional parameter space and assessing the impact of each parameter on E_g. The goal is to determine whether adjusting the XC parameters can align with experimental bandgap values and identify a functional tailored to specific materials.

Rather than seeking a universal XC functional, this study focuses on customizing the SCAN functional for specific materials. Given the inherent differences among materials, we explore a system-specific reparameterization approach, referred to as system-dependent SCAN (SD-SCAN) a structure-conditioned variant of SCAN in which a small set of internal SCAN parameters is manually adjusted to optimize bandgap predictions.

Additionally, machine learning algorithms predict SCAN parameters from material properties such as crystal structure, density, electronegativity, and covalency. In practice, parameters are optimized on a training subset and then predicted for new materials via an ML mapping from structural/electronic descriptors, making the procedure algorithmic (system dependent) at deployment. Unlike previous ML studies, which either predict bandgaps directly or the XC enhancement factors, this approach uses experimental bandgap data to reparameterize SCAN. The ML model then predicts the appropriate internal parameters for a specific material based on its physical properties. This approach establishes a connection between the physical properties of solids and the internal parameters of the XC functional, thereby enabling SCAN to describe electronic properties accurately.

The SCAN semilocal density functional, introduced in 2015 by Jianwei Sun, Adrienn Ruzsinszky, and John P. Perdew [11], is a nonempirical meta-GGA constructed via a constraint-guided design strategy that satisfies known exact conditions and appropriate norms to achieve reliable and transferable performance across diverse bonding environments. This framework leads to an improved treatment of bandgaps and dispersion interactions, a more balanced description of exchange and correlation, and a partial reduction of self-interaction errors. Enhanced performance for some systems with d- and f-electrons is thus an outcome of this design. Owing to these strengths, SCAN has increasingly replaced PBE in high-throughput frameworks for predicting novel materials, including its adoption in recent large-scale discovery efforts [47, 48].

The SCAN XC functional is written as:

$$E_{xc}[n] = \int n\, \varepsilon_{xc}(n, \nabla n, \tau)\, d^3r, \tag{1}$$

where n is the electronic density, ∇n is the gradient of the electronic density, and $\tau = \sum_i^{occ} \frac{1}{2}|\nabla \psi_i|^2$ is the kinetic energy density. The dimensionless density gradient s and variable α are calculated as:

$$s = \frac{|\nabla n|}{2(3\pi^2)^{1/3} n^{4/3}}, \tag{2}$$

$$\alpha = \frac{\tau - \tau^W}{\tau^{\text{unif}}}, \tag{3}$$

where $\tau^W = |\nabla n|^2/8n$ is the single orbital limit of τ and $\tau^{\text{unif}} = (3/10)(3\pi^2)^{2/3} n^{5/3}$ is the uniform density limit. The variable α characterizes bond strength: $\alpha = 0$ for covalent bonds, $\alpha = 1$ for metallic bonds, and $\alpha > 1$ for weak bonds. The exchange energy is defined as:

$$E_x[n] = \int n\, \varepsilon_x^{\text{unif}}(n)\, F_x(s,\alpha)\, d^3r, \tag{4}$$

where $\varepsilon_x^{\text{unif}}(n) = -(3/4\pi)(3\pi^2 n)^{1/3}$ is the exchange energy per particle of the uniform electron gas, and $F_x(s,\alpha) = h_x^\alpha\, g_x(s)$ is the exchange enhancement factor. In the case of fully metallic bonds, h_x^1 acquires a PBE-like form of the exchange enhancement factor:

$$h_x^1 = 1 + \kappa - \frac{\kappa}{1 + x/\kappa}, \tag{5}$$

with

$$x = \mu s^2 \left[1 + \frac{b_4 s^2}{\mu} e^{-|b_4| s^2/\mu}\right] + \left[b_1 s^2 + b_2 (1-\alpha) e^{-b_3 (1-\alpha)^2}\right]^2, \tag{6}$$

where $\mu = 10/81$, $b_1 = (511/13500)/(2b_2)$, $b_2 = (5913/405000)^{1/2}$, $b_3 = 0.5$, and $b_4 = \mu^2/\kappa - 1606/18225 - b_1^2$. In the case of pure covalent bonding, the creators of SCAN imposed a strongly tightened bound $F_x \leq 1.174$, where $h_x^0 = 1.174$ and $g_x(s) = 1 - \exp[-a_1 s^{-1/2}]$, with $a_1 = 4.9479$ to fit the exact exchange energy of the hydrogen atom. The exchange enhancement factor $F_x(s,\alpha)$ is calculated as the interpolation between $\alpha = 0$ and $\alpha \approx 1$ or the extrapolation when $\alpha \to \infty$. It is given by:

$$F_x(s,\alpha) = \left\{h_x^1(s,\alpha) + f_x(\alpha)[h_x^0 - h_x^1(s,\alpha)]\right\} g_x(s), \tag{7}$$

where $f_x(\alpha)$ is the interpolation/extrapolation factor, defined as:

$$f_x(\alpha) = \exp\left[\frac{-c_{1x}\alpha}{1-\alpha}\right]\theta(1-\alpha) - d_x \exp\left[\frac{c_{2x}}{1-\alpha}\right]\theta(\alpha - 1). \tag{8}$$

Here $\theta(x)$ is a step function that activates the left side of Equation 8 when $\alpha \leq 1$ and the right side when $\alpha > 1$.

The correlation energy is defined as:

$$E_c[n] = \int n\, \varepsilon_c(r_s, \zeta, s, \alpha)\, d^3r, \tag{9}$$

where $\zeta = (n_\uparrow - n_\downarrow)/(n_\uparrow + n_\downarrow)$ is the spin polarization and $r_s = (4\pi n/3)^{-1/3}$ is the Wigner–Seitz radius. Similarly to the exchange, the correlation energy per electron ε_c is constructed as an interpolation between $\alpha = 0$ and $\alpha \approx 1$, and an extrapolation when $\alpha \to \infty$ as:

$$\varepsilon_c = \varepsilon_c^1 + f_c(\alpha)[\varepsilon_c^0 - \varepsilon_c^1], \tag{10}$$

where $f_c(\alpha)$ is the interpolation/extrapolation factor given by:

$$f_c(\alpha) = \exp\left[\frac{-c_{1c}\alpha}{1-\alpha}\right]\theta(1-\alpha) - d_c \exp\left[\frac{c_{2c}}{1-\alpha}\right]\theta(\alpha - 1). \tag{11}$$

The SCAN XC functional comprises seven parameters, divided into four for exchange ($\kappa = 0.065$, $c_{1x} = 0.667$, $d_x = 1.24$, and $c_{2x} = 0.8$) and three for correlation ($c_{1c} = 0.64$, $d_c = 0.7$, and $c_{2c} = 1.5$). The parameter κ is associated with the metallic nature of the compound, while c_{1x} and c_{1c} are linked to bond strength. The parameters d_x, c_{2x}, d_c, c_{2c} are related explicitly to weak bonds, including van der Waals (vdW) bonds and regions characterized by very low electronic density. It is important to note that these parameters act synergistically within the SCAN framework; adjusting one parameter inevitably affects the others and the overall XC behavior.

The seven parameters of SCAN were determined by enforcing exact constraints and by fitting to three appropriate norms: (i) the jellium surface XC energy, (ii) the large-Z asymptotic coefficients of the exchange and correlation energies of rare-gas atoms, and (iii) the binding-energy curve of the compressed Ar_2 dimer. Varying the parameters associated with these norms affects the description of these specific reference systems; however, it does not alter the exact constraints satisfied by SCAN, which remain unaltered. In this work, the SCAN functional is selectively modified for application to semiconductors and insulators, with no attempt to describe metallic systems or jellium-like models. The primary goal of SD-SCAN is to improve the prediction of electronic bandgaps, while structural properties such as lattice constants are also preserved through constrained optimization.

II. RESULTS

Initially, we explore the κ-c_{1x} space for 20 significant semiconductors and insulators. Figure 1 illustrates E_g variation across the κ-c_{1x} space for carbon, silicon, and germanium, all in the diamond cubic phase. Notably, a maximum bandgap exists in the κ-c_{1x} plane, with its location varying among materials. While carbon's maximum E_g is smaller than the experimental value, silicon and germanium exhibit various combinations of κ and c_{1x} that match the experimental values.

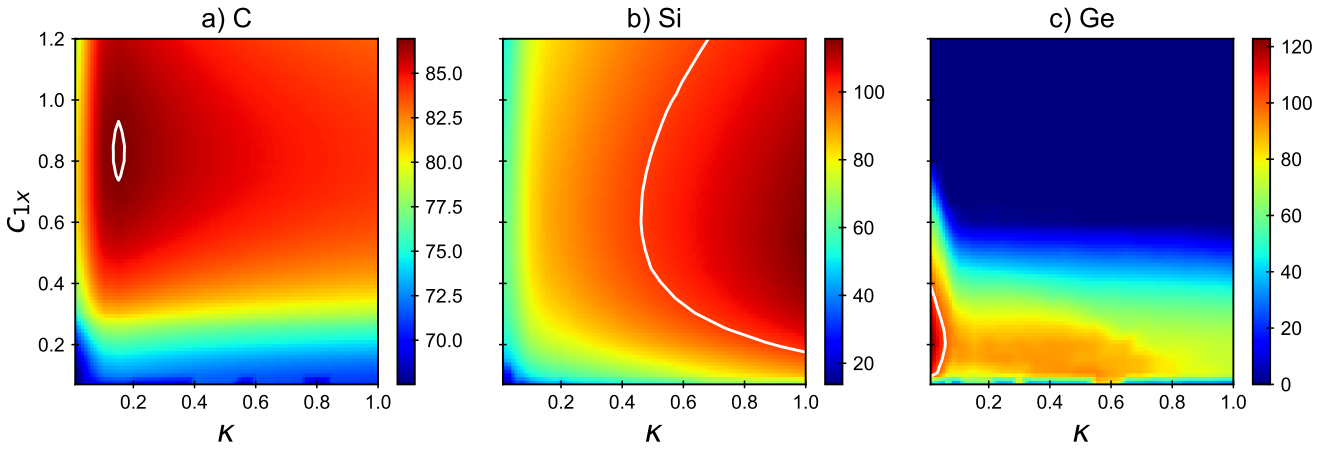

FIG. 1. **Bandgap variation across the κ–c_{1x} space.** Color maps show the predicted electronic bandgap E_g as a function of κ and c_{1x} for: (a) carbon diamond, (b) silicon, and (c) germanium. For carbon, the white line encloses the region with the maximum bandgap. For silicon and germanium, the white line represents all the solutions that achieve the experimental bandgap. The color bar reports E_g as a percentage of the experimental value. Warmer (cooler) colors denote larger (smaller) bandgaps.

Additional constraints are introduced to refine solutions. First, lattice parameters are incorporated as constraints, enabling the selection of optimal E_g solutions with lattice parameters closer to experimental values. Second, considering the structure of Equation 8, weak bonds can be characterized by adjusting d_x while maintaining c_{2x} constant. Third, numerous calculations with various materials show that d_c and c_{2c} have no impact on E_g or lattice parameters. These considerations allow us to reduce the problem to a 4-dimensional parameter space for bandgap optimization: κ, c_{1x}, d_x, and c_{1c}.

Diamond-like structures: Figure 2 presents the lattice parameter behavior across the κ-c_{1x} plane for carbon diamond, silicon, and germanium. The plotted lines represent all possible solutions based on experimental lattice parameters. Notably, for carbon diamond, the line coincides with the point of maximum bandgap observed in the κ-c_{1x} plane. This implies that adjusting κ to 0.15 and c_{1x} to 0.85 can enhance the bandgap from 4.56 eV (with traditional SCAN) to 4.70 eV while maintaining accurate lattice parameters. Given that d_x signifies weak bonds or regions with very low electronic density, it is reasonable to decrease it for carbon diamond, which comprises perfect covalent bonds between carbon atoms, but not to increase it. A slight increase in E_g is observed concerning d_x, while the lattice parameters significantly increase. Conversely, reducing c_{1c} results in a notable increase in the bandgap without affecting the lattice parameters. Further exploration of the d_x-c_{1c} space indicates that the optimal solution is $d_x = 1.00$ and $c_{1c} = 0.1$, resulting in a maximized bandgap of 5.02 eV with accurate lattice parameters. This represents the highest bandgap prediction for carbon diamond among the semilocal DFT functionals considered here. It is worth noting that achieving the experimental bandgap for materials such as carbon diamond is currently unattainable with the current form of the SCAN XC functional.

Comparing Figures 1b and 2b shows that no solution satisfies the experimental bandgap and lattice parameters simultaneously for silicon. The optimal solution for experimental E_g involves setting κ to 0.5 and c_{1x} to 0.45, with lattice parameters closest to the experimental values. Parameter d_x influences both E_g and lattice constants, increasing concurrently with its rise. Conversely, c_{1c} exhibits a convex curve, leading to E_g augmentation as it deviates from the default value while leaving the lattice parameters unaffected. The most favorable solution for silicon sets d_x to 0.9 and c_{1c} to 0.1, resulting in E_g matching the experimental value with a lattice parameter of 5.47 Å (error +0.04 Å).

Achieving the experimental E_g for germanium is feasible with lattice parameters that closely approximate experimental values, albeit slightly smaller. The optimal solution requires small values for the κ (0.05) and c_{1x} (0.15) parameters. Unlike carbon and silicon, germanium's bandgap decreases with an increasing d_x, while the lattice parameters increase. Additionally, E_g increases with c_{1c}, while the lattice parameters decrease slightly. Despite the absence of weak vdW forces, germanium can still exhibit regions of low electronic density due to its larger atomic radius relative to carbon and silicon. Consequently, increasing d_x to expand the cell towards optimal parameters is physically justified. The most effective solution sets d_x to 1.6 and c_{1c} to 0.91, achieving both the experimental bandgap and lattice parameters.

Noble gases: Under ambient conditions, noble gases exist as monoatomic gases with minimal reactivity, but at near absolute zero temperatures, they form face-centered

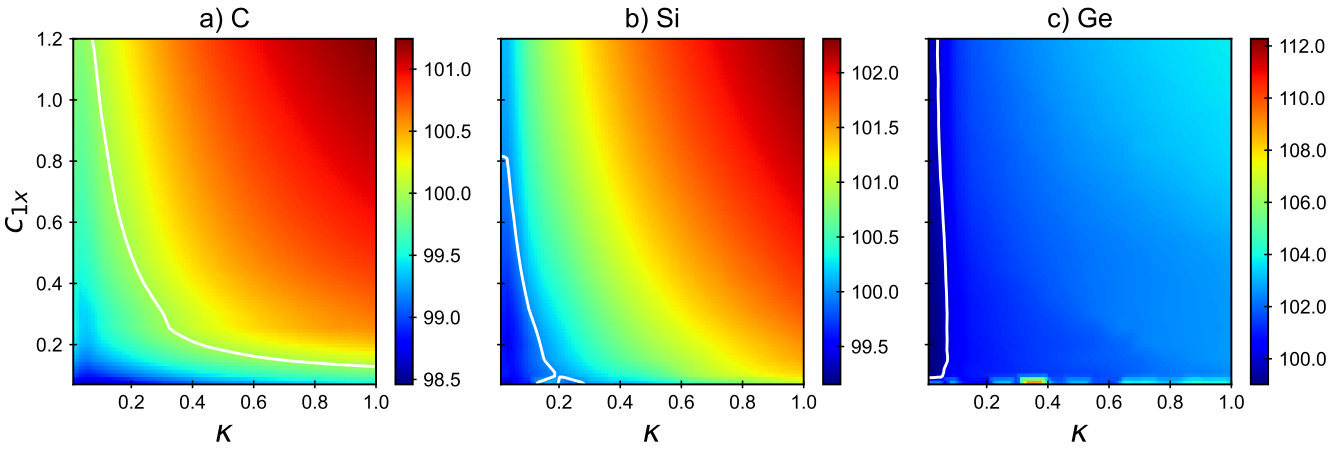

FIG. 2. **Lattice parameter across the κ–c_{1x} space.** Color maps show the relaxed cubic lattice parameter (a in Å) as a function of κ and c_{1x} for: (a) carbon diamond, (b) silicon, and (c) germanium. The white curve represents the solutions that achieve the experimental lattice parameters in all cases. The color bar reports a as a percentage of the experimental value. Warmer (cooler) colors denote larger (smaller) bandgaps.

TABLE I. Bandgap values (eV) and lattice parameters (Å) of representative solids obtained using different exchange–correlation functionals. Materials are grouped by crystal system (CS): diamond-like (diam), face-centered cubic (fcc), rocksalt (rs), zincblende (zb), and hexagonal (hex). For cubic structures, only the a-lattice parameter is reported, while for hexagonal structures both a- and c-lattice parameters are provided. The optimized parameters (κ, c_{1x}, d_x, and c_{1c}) correspond to the values used in the SD-SCAN functional for each material. The last row reports the average mean absolute error (MAE), excluding noble gases.

		Bandgap (eV)				Lattice Parameters (Å)				Parameters			
Material	CS	PBE	SCAN	SD-SCAN	Expt.	PBE	SCAN	SD-SCAN	Expt.	κ	c_{1x}	d_x	c_{1c}
C	diam	4.12	4.58	5.02	5.40 [1]	3.57	3.56	3.57	3.57 [1]	0.15	0.85	1	0.1
Si	diam	0.62	0.84	1.17	1.17 [1]	5.47	5.43	5.47	5.43 [1]	0.50	0.45	0.9	0.1
Ge	diam	0.00	0.15	0.74	0.74 [1]	5.75	5.66	5.67	5.66 [1]	0.05	0.15	1.6	0.91
Ne	fcc	11.58	13.30	21.46	21.48 [49]	4.46	3.98	4.35	4.46 [1]	0.01	0.2	9	0.64
Ar	fcc	8.46	9.54	14.11	14.15 [49]	5.76	5.26	7.10	5.31 [1]	0.01	0.2	8	0.64
Kr	fcc	7.17	8.01	11.60	11.59 [49]	6.38	5.75	7.31	5.64 [1]	0.01	0.2	6.3	0.64
Xe	fcc	6.21	6.90	9.28	9.29 [49]	7.01	6.36	8.61	6.13 [1]	0.01	0.2	4	0.64
CdO	rs	0.00	0.00	0.80	0.80 [50]	4.78	4.71	4.77	4.70 [51]	0.17	0.15	1.24	0.64
LiCl	rs	6.29	7.51	7.81	9.40 [52]	5.14	5.08	5.16	5.11 [52]	0.01	0.35	1.24	0.64
LiF	rs	8.94	10.64	11.67	13.60 [53]	4.05	3.97	3.97	4.01 [52]	0.01	0.1	1.24	0.64
MgO	rs	4.49	5.64	6.61	7.67 [53]	4.25	4.20	4.18	4.20 [1]	0.01	0.2	1.24	0.64
GaAs	zb	0.15	0.64	1.52	1.52 [1]	5.75	5.67	5.65	5.65 [1]	0.027	0.15	1.24	0.64
β-SiC	zb	1.51	1.86	2.30	2.30 [50]	4.38	4.35	4.34	4.35 [1]	0.15	0.2	1.6	0.64
ZnS	zb	2.01	2.71	3.54	3.54 [50]	5.45	5.37	5.40	5.41 [1]	0.02	0.1	1.8	0.64
c-BN	zb	4.45	4.97	5.52	6.36 [54]	3.63	3.61	3.58	3.62 [52]	0.15	0.1	1.6	0.64
MgS	zb	3.39	4.17	5.39	5.40 [52]	5.69	5.65	5.90	5.62 [52]	1.00	0.45	1.6	0.64
α-SiC	hex	2.03	2.38	2.86	2.86 [50]	3.09, 15.18	3.08, 15.09	3.07, 15.08	3.08, 15.12 [55]	0.15	0.15	1.9	0.64
GaN	hex	1.71	2.23	3.34	3.34 [50]	3.22, 5.24	3.19, 5.20	3.14, 5.09	3.14, 5.72 [56]	0.03	0.1	0.8	0.64
MoS_2	hex	1.54	1.29	1.23	1.23 [57]	3.18, 14.08	3.18, 12.79	3.17, 12.65	3.17, 12.32 [58]	0.08	0.1	1.4	0.64
h-BN	hex	4.59	4.81	5.95	5.96 [54]	2.51, 7.80	2.50, 6.77	2.51, 8.28	2.54, 6.60 [59]	0.15	0.1	3.6	0.64
MAE		1.63	1.07	0.36		0.04, 0.87	0.02, 0.30	0.04, 0.67					

cubic (fcc) structures primarily influenced by vdW forces. The original SCAN paper evaluated Ne, Ar, Kr, and Xe for XC energy prediction [11]. Subsequently, E_g prediction for Kr and Ar was investigated using the TASK XC functional [32].

Given the significance of these elements and their reliance on van der Waals (vdW) interactions, parameter optimization for bandgap prediction is performed. A consistent trend emerges across all cases: E_g is maximized with small values of κ (0.01) and c_{1x} (0.2), resulting in a 10% improvement in bandgap prediction compared to traditional SCAN.

The effect of d_x, essential for weak vdW bonds, is examined to match experimental values. Increasing this parameter by one order of magnitude—Ne: 9, Ar: 8, Kr: 6.3, Xe: 4—is necessary to match experimental bandgap values. Nevertheless, this adjustment results in excessive cell expansion, which is more pronounced in larger elements. This highlights the significant influence of d_x on weak bonds and emphasizes the need for careful fitting tailored to specific materials.

In contrast, c_{1c} has a positive but minor effect on E_g, with no significant change in lattice parameters. The diminished influence of correlation on E_g and lattice parameters in noble gases stems from their closed-shell electron configurations, resulting in localized electron densities [1]. This localization reduces the impact of correlation effects compared to systems with more delocalized electrons.

Ionic crystals: As shown in Table I, ionic crystals (LiF, LiCl, MgO, CdO) exhibit very small κ (0.01) and an average c_{1x} of 0.2, similar to noble gases. This corresponds to the closed electronic shells of ions in simple ionic crystals, identical to those in inert gas atoms [1].

However, unlike noble gases, ionic crystals lack weak van der Waals (vdW) forces, and regions of low electron density are not expected. Consequently, increasing d_x results in minimal changes in E_g and lattice parameters. Additionally, the spherically symmetric charge distribution makes correlation effects less pronounced than exchange effects. Varying c_{1c} shows minimal increases in E_g and lattice parameters, as expected.

The current form of SCAN does not accurately predict the bandgap of highly ionic materials. This limitation arises mainly from the definition of α in Equation 3. In these solids, the valence charge is strongly localized on the anions but in a nearly spherical, multi–orbital distribution. Such regions are characterized by τ differing significantly from the single–orbital limit τ^{W} but being comparable to the uniform limit τ^{unif}, so that the band-edge states sample $\alpha \approx 1$ and $\alpha > 1$ much more than $\alpha \approx 0$. This behavior contrasts with covalent semiconductors (like Si), whose bonding charge density is concentrated in single–orbital bonds and is therefore dominated by $\alpha \approx 0$.

In SCAN, the exchange enhancement factor $F_x(s, \alpha)$ varies only weakly with α near $\alpha \approx 1$ (i.e., $\partial F_x/\partial\alpha \to 0$), so the GKS potential lacks a large derivative–discontinuity–like response in precisely the regime that is most important for highly ionic and charge–transfer solids. Reparametrizing κ and c_{1x} therefore has a limited impact on the bandgaps of ionic crystals: even after optimization, SCAN captures only about 80–85% of the experimental E_g in the studied materials. Meta–GGAs that strengthen the α-dependence near $\alpha \approx 1$ (e.g., TASK [32, 60]) can already improve the description of ionic crystals at a semilocal computational cost.

Residual self–interaction and the absence of long–range nonlocal (Hartree–Fock–like) exchange in semilocal SCAN further contribute to the underestimation of bandgaps in these strongly charge-separated systems [28, 61]. Hybrid functionals and GW approaches with explicit nonlocal exchange can yield further improvements, but at a significantly higher computational cost.

Zincblende structures: This structure comprises two fcc lattices, each shifted by a quarter of a body diagonal, with each element positioned on a separate fcc lattice. Covalent bonds among the various components characterize this structure. Observations from Table I reveal that most zincblende structures exhibit small values of κ, similar to diamond-like structures. However, MgS stands out, requiring maximization of κ to achieve the experimental bandgap, resulting in a 0.3 Å increase in lattice parameters. In all cases, c_{1x} remains consistently smaller than the default value, as observed for germanium and silicon.

Due to differences in atomic size within covalent bonds, areas of low electronic density emerge, evidenced by an increase in E_g and lattice parameters with higher values of d_x. Consequently, there is a physical motivation to adjust d_x to achieve the desired E_g and lattice parameters; however, for c-BN, minor corrections in d_x fall short. While c-BN achieves an 86% bandgap through κ and c_{1x} reparametrization, lattice parameters remain slightly below experimental values. Increasing d_x aims to rectify both effects; however, as with carbon diamond, minimal changes are observed due to strong covalent bonds and the presence of a few regions of low electronic density.

Additionally, c_{1c} demonstrates sensitivity to E_g with a positive slope in all cases, although it has a minimal impact on lattice parameters for most zincblende materials.

Hexagonal structures: Table I shows that most hexagonal structures have small κ values, peaking at 0.15, and c_{1x} around 0.1, similar to diamond-like and zincblende structures. Materials with the same chemical formula but different crystal structures, such as α-SiC, β-SiC, c-BN, and h-BN, exhibit similar κ and c_{1x}. This suggests that the bonding environment determines these parameters, with electronic density within bonds directly influencing the optimal values.

This relationship extends to 2D materials, as seen in MoS_2, where extrapolating bulk parameters to the monolayer yields a bandgap of 1.87 eV and a lattice parameter of 3.16 Å, closely matching experimental values. This suggests the potential transferability of κ and c_{1x} parameters to 2D materials.

Increasing d_x in hexagonal structures generally increases E_g, with materials like MoS_2 and h-BN showing larger changes due to vdW forces. Additionally, d_x typically increases lattice parameters, but the accuracy of the a- and c-lattice parameters differs: the former closely matches experimental values, whereas the latter is often overestimated or underestimated. Despite testing various

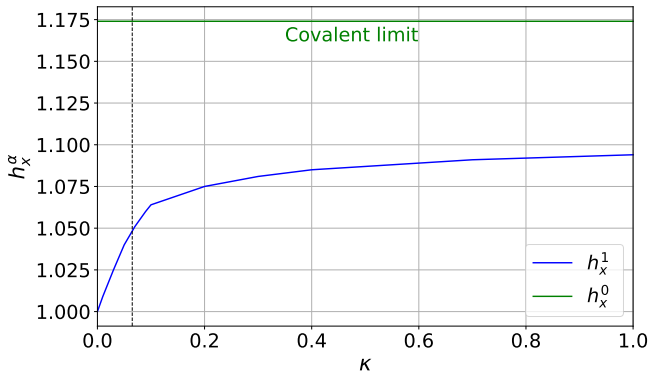

FIG. 3. **Variation of h_x^α as a function of κ.** Curves show the behavior of h_x^1 (blue) and h_x^0 (green) as a function of κ for fixed s=1. Default κ showed as a dashed line. The value of h_x^α lies between h_x^1 and h_x^0 and depends on α.

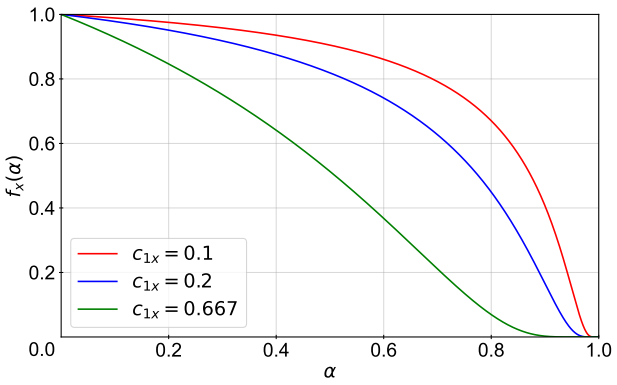

FIG. 4. **Dependence of the interpolation factor $f_x(\alpha)$ on c_{1x}.** Curves show f_x versus α for different values of c_{1x}: 0.1 (red), 0.2 (blue), and 0.667 (green; SCAN default).

κ-c_{1x}-d_x combinations, no parameter set simultaneously achieves exact accuracy for both lattice parameters. Parameter c_{1c} usually exhibits a positive slope with minimal impact on lattice constants, which is consistent with previous findings.

General Findings: The materials in Table I show κ ranging from 0.01 to 0.17, with modes at 0.01 and 0.15. These values fluctuate around the default SCAN value of 0.065, which is near the midpoint of this range. The behavior of the bandgap varies with κ: it can be maximized at minimal values (e.g., germanium), peak around 0.15 with a concave shape (e.g., carbon diamond), or be maximized at larger values close to 1 (e.g., silicon). Increasing κ towards 1 consistently leads to excessive cell expansion, making high values undesirable. Additionally, smaller values of κ result in small values of h_x^1 according to Equation 5. As shown in Figure 3, when κ increases, h_x^1 rises, narrowing the gap between h_x^1 and h_x^0. Here, h_x^0 is the covalent limit, while h_x^1 represents a fully metallic bond. When h_x^1 approaches h_x^0, the material is treated as fully covalent, regardless of changes in α across the electronic density. This observation is consistent with the principle that covalent materials generally exhibit larger interatomic distances than metals. Metallic structures feature closely packed arrangements with relatively short interatomic distances. In contrast, covalent bonds are directional, leading to a more diffuse electron distribution and larger average distances between atoms.

By contrast, c_{1x} exhibits a consistent pattern, remaining relatively uniform across most materials and typically peaking at small values. As shown in Table I, its average value is 0.225, with modes at 0.2, 0.1, and 0.15. Unlike κ, the default SCAN value of c_{1x}, 0.667, appears notably high for accurately describing the electronic behavior of semiconductors and insulators. As shown in Figure 4, smaller c_{1x} values in Equation 8 produce a flatter curve for the interpolation factor $f_x(\alpha)$, resulting in more gradual changes with α. Conversely, higher c_{1x} values yield a steeper curve, causing more pronounced variations. Although c_{1x} solely alters the shape of the exponential term in Equation 8, it is reasonable that for semiconductors and insulators, c_{1x} assumes smaller values than the default. This is because, during screening across different electronic-density regions and varying α values, the interpolation factor tends to be higher, thereby promoting covalent behavior over metallic behavior. Consequently, this increases the exchange enhancement factor F_x and the solid's bandgap. By contrast, for ionic semiconductors whose band-edge states predominantly probe α close to 1, the variation of $f_x(\alpha)$ with c_{1x} is much weaker, so the impact on the exchange interpolation factor, and hence on the bandgap, is minimal, consistent with Figure 4 and the preceding discussion of ionic crystals.

Parameter d_x increases the bandgap in materials with regions of low electronic density or vdW forces. Increasing it generally increases the lattice parameters, but larger values result in excessive cell expansion.

The findings reveal that bandgaps in covalent materials are significantly sensitive to c_{1c}, while they have minimal impact on noble gases and ionic crystals. Generally, c_{1c} has minimal effects on lattice parameters, making the exchange component the primary factor in accurate predictions. Overall, exchange interactions are more influential than correlation effects in modulating E_g, as observed in other studies [62].

As depicted in Table I, SD-SCAN, defined as the SCAN functional with optimal parameters, systematically improves bandgap predictions relative to PBE and SCAN for most materials while retaining accurately described lattice parameters. The most significant residual discrepancies in E_g occur for highly ionic rocksalt compounds, consistent with the SCAN functional's limitations in such systems. For lattice parameters, SCAN and SD-SCAN both reproduce experimental values to high accuracy, indicating that the bandgap improvement achieved by SD-SCAN does not require a substantial deterioration of equilibrium structural properties, in line with the observations of Kovács et al [34]. To further ex-

amine these trends, the following paragraphs analyze the effects of SD-SCAN on band structures, charge density, and optical properties.

Band structures: Figure 5 illustrates the band structures of carbon diamond and GaAs across PBE, SCAN, and SD-SCAN XC potentials. While the overall shapes of the bands are similar, the three XC potentials lead to different bandgaps and bandwidths. PBE bands are slightly higher in energy than SCAN and SD-SCAN, which are closely aligned. The conduction band shifts upward from PBE to SCAN, and then from SCAN to SD-SCAN. Using SD-SCAN, carbon diamond shows an indirect bandgap of 5.02 eV, and GaAs shows 1.52 eV, both consistent with experimental values.

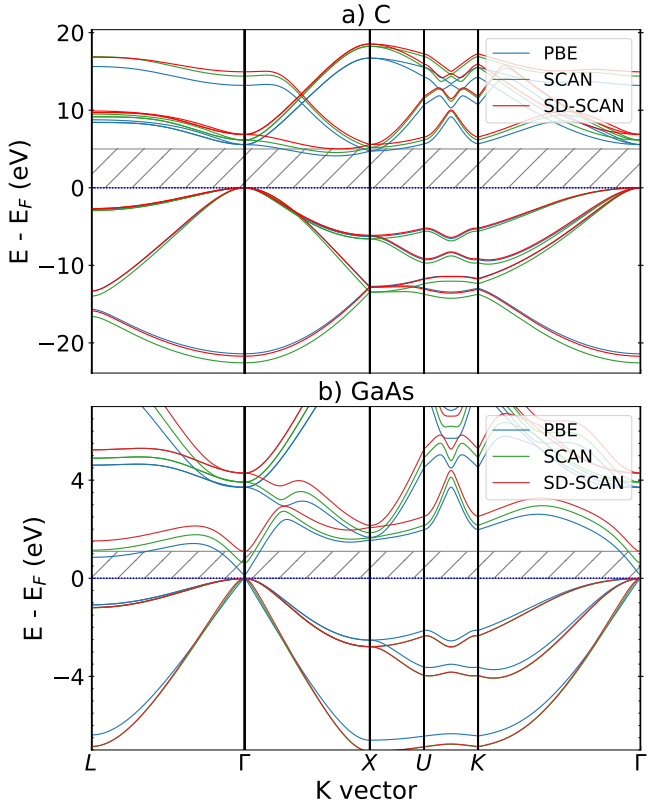

FIG. 5. **Band structures with different exchange–correlation functionals.** (a) Carbon (diamond). (b) GaAs. Curves colors denote functionals: PBE (blue), SCAN (green), and SD-SCAN (red). The hatched region visually indicates the experimental fundamental bandgap. (Image generated with PyProcar[63, 64].)

Charge density: The electron density and electron localization function (ELF) are analyzed for carbon diamond, silicon, CdO, and GaAs using LDA, PBE, SCAN, and SD-SCAN. As shown in Figure 6, in carbon diamond, SD-SCAN enhances charge localization along C–C bonds and broadens the electron distribution relative to other functionals, reflecting strong covalent bonding. A similar effect occurs in silicon, where SD-SCAN produces pronounced Si–Si bond localization with a cylindrical profile.

For CdO, an ionic material, the charge density remains spherical and is centered on the Cd and O atoms for all functionals, with minimal variation. The ELF indicates electron accumulation near the O atoms due to their higher electronegativity.

In GaAs, charge density is predominantly localized near As atoms. SD-SCAN increases the charge density between Ga–As bonds, accentuating their covalent character (see Supplementary Figure 2).

Overall, SD-SCAN expands the charge density in covalent materials, thereby reducing electron–electron repulsion energy. In contrast, changes remain minimal in ionic systems, highlighting the limitations of semilocal functionals in accurately capturing their electronic structure.

Optical properties: The electron bandgap plays a crucial role in a solid's optical properties, particularly in determining the energies of the photons it can absorb or emit. When photons with energies near or above the bandgap are absorbed, they can excite electrons from the valence band to the conduction band, generating electron-hole pairs. This process influences optical properties, including reflectance, transmittance, and refractive index. The optical dielectric constant $\epsilon(\infty)$, related to the refractive index, reflects the material's response to high-frequency electric fields.

The dielectric function follows an inverse quadratic dependence on the interband transition energy [66]; thus, bandgap underestimation in PBE and SCAN leads to excessive screening and overestimated $\epsilon(\infty)$. Adjusting internal parameters in SD-SCAN reduces screening, thereby yielding a more accurate optical dielectric constant.

The impact of bandgap correction on optical properties is evaluated by computing the optical dielectric constant using the finite electric field response method. As shown in Table II, PBE systematically overestimates the dielectric constant, while SCAN improves accuracy. SD-SCAN slightly underestimates values but offers better predictions than SCAN in 42% of cases. SCAN fails for 11% of materials by misclassifying them as metals (e.g., Ge, InAs, and GaSb), thereby making dielectric calculations infeasible. In contrast, SD-SCAN correctly reproduces finite values for all systems, enabling reliable dielectric predictions where SCAN fails.

Figure 7 compares the dielectric function of silicon calculated with various XC functionals against experimental data. In the real part of the dielectric function, PBE shows a leftward shift of about 0.7 eV, leading to a 65% average relative error. SCAN shifts by 0.2 eV and SD-SCAN by 0.1 eV, with SD-SCAN (40%) slightly outperforming SCAN (46%). The imaginary part follows a similar trend: PBE exhibits a significant leftward shift, with a 383% error, while SCAN and SD-SCAN align their curves more accurately. SCAN captures the highest peak

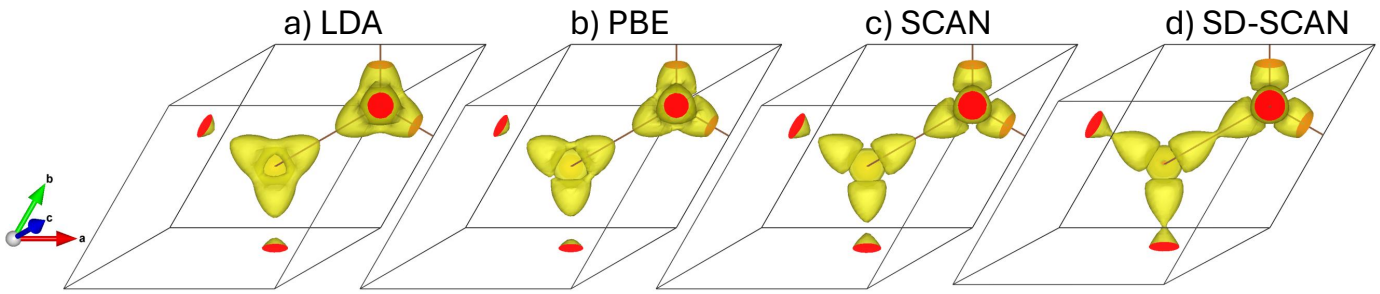

FIG. 6. **Charge density with different exchange–correlation functionals for carbon diamond.** Charge density distribution for (a) LDA, (b) PBE, (c) SCAN, and (d) SD-SCAN. (Images generated with VESTA at an isosurface level of 0.251357 [65].)

TABLE II. Optical dielectric constants, $\epsilon(\infty)$, of representative solids obtained using different exchange–correlation functionals. Experimental values are taken from Ref. [1]. Mean error and mean absolute error are reported for comparison. Average values exclude materials classified as metals.

	$\epsilon(\infty)$				Mean Absolute Error			Mean Error		
Material	Expt.	PBE	SCAN	SD-SCAN	PBE	SCAN	SD-SCAN	PBE	SCAN	SD-SCAN
C	5.50	5.44	5.31	5.90	0.06	0.19	0.40	-0.06	-0.19	0.40
Si	11.70	12.86	11.43	10.98	1.16	0.27	0.72	1.16	-0.27	-0.72
Ge	15.80	metal	17.51	14.01		1.71	1.79		1.71	-1.79
LiBr	3.20	3.39	3.22	3.07	0.19	0.02	0.13	0.19	0.02	-0.13
LiCl	2.70	2.91	2.81	2.67	0.21	0.11	0.03	0.21	0.11	-0.03
RbI	2.60	2.67	2.60	2.42	0.07	0.00	0.18	0.07	0.00	-0.18
LiF	1.90	2.00	1.96	1.89	0.10	0.06	0.01	0.10	0.06	-0.01
KCl	2.10	2.23	2.20	2.11	0.13	0.10	0.01	0.13	0.10	0.01
AgBr	4.60	5.91	5.41	3.40	1.31	0.81	1.20	1.31	0.81	-1.20
AgCl	4.00	4.94	4.59	3.04	0.94	0.59	0.96	0.94	0.59	-0.96
MgO	2.95	3.28	3.02	2.94	0.33	0.07	0.01	0.33	0.07	-0.01
GaP	8.50	10.29	9.48	7.72	1.79	0.98	0.78	1.79	0.98	-0.78
GaAs	10.90	14.06	12.20	9.75	3.16	1.30	1.15	3.16	1.30	-1.15
β-SiC	6.70	7.13	6.67	6.37	0.43	0.03	0.33	0.43	-0.03	-0.33
InAs	12.30	metal	metal	11.08			1.23			-1.23
InP	9.60	11.00	9.49	8.07	1.40	0.11	1.53	1.40	-0.11	-1.53
GaSb	14.40	metal	metal	12.17			2.23			-2.23
TlBr	5.40	5.73	5.56	4.84	0.33	0.16	0.56	0.33	0.16	-0.56
TlCl	5.10	5.09	4.99	4.96	0.01	0.11	0.14	-0.01	-0.11	-0.14
Average					0.73	0.31	0.51	0.72	0.22	-0.46

but not the smallest one (103% error), whereas SD-SCAN captures both peaks with the lowest error (64%).

These results demonstrate that bandgap correction enhances the accuracy of optical property calculations. However, the dielectric response depends not only on the bandgap but also on the XC kernel, which influences screening and varies across functionals [67]. Additionally, the absence of excitonic effects at the meta-GGA level contributes to discrepancies with experimental spectra, particularly in peak positions and shapes [68, 69]. Despite this, SD-SCAN provides a modest yet consistent improvement over SCAN, yielding values closer to experiment without altering the overall spectral shape. This trend aligns with previous findings with hybrid functionals, in which bandgap corrections improve agreement with optical measurements [70].

Machine Learning: To improve E_g predictions, a system-dependent ML-driven XC functional (ML-SCAN) is developed, enabling parameter fitting based on material-specific descriptors. A rapid scan over the κ-c_{1x} space is performed on 244 materials: first, fixing κ to find the best c_{1x}, then varying κ for optimal pairing.

Based on these findings, we develop a machine learning method to predict κ and c_{1x} using the physical properties of solids as input variables. These properties include space group, period (related to the rows in the periodic table), valency (related to the columns in the periodic table), electronegativity (X), covalency, bond strength, ionic density (atoms/volume), electronic density (electrons/volume), and mass density. Covalency can be defined as $\exp[-0.25(X_A - X_B)^2]$, where X_A and X_B are the electronegativities of the elements involved in the chemical bonding. Bond strength is calculated as cova-

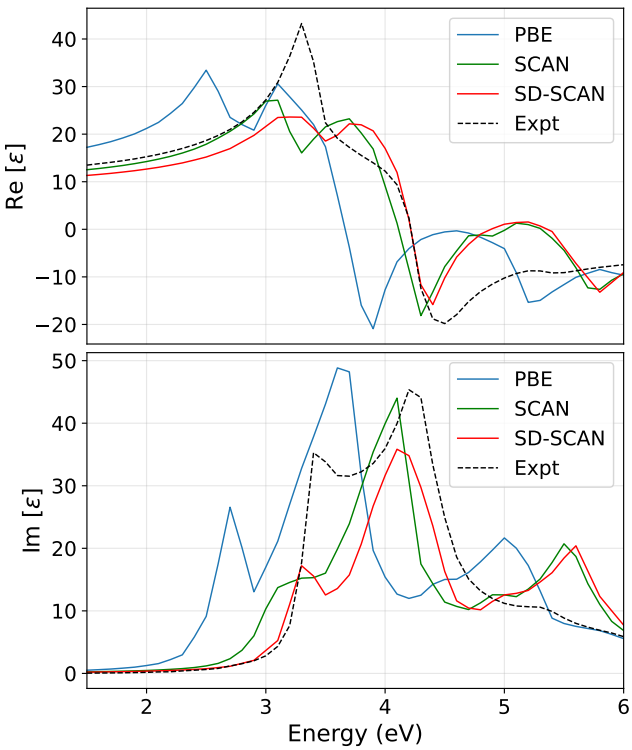

FIG. 7. **Dielectric function with different exchange-correlation functionals.** Real (top) and imaginary (bottom) part of the dielectric function of silicon. Spectra computed with PBE (blue), SCAN (green), and SD-SCAN (red). Experimental data from Ref. [71] is shown for comparison (black dashed line).

lency divided by the atomic distance between the bonded atoms. All descriptors used are either tabulated atomic properties or directly computable from first-principles-relaxed structures.

Supervised learning regression algorithms, including Multiple Linear Regression (MLR), K-Nearest Neighbors (KNN), Decision Trees (DT), Random Forest (RF), AdaBoost (ADA), and Gradient Boosting Regressor (GBR), are employed to develop models that predict κ and c_{1x}.

The optimal algorithm was selected based on three criteria: (1) Out-of-sample accuracy (MAE and σ of κ and c_{1x}): RF, MLR, and ADA achieved the lowest combined mean absolute error and standard deviation (Supplementary Table 2); (2) Coverage Probability: MLR yielded prediction intervals closest to the 95% target, followed by ADA and RF (Supplementary Table 3); (3) Overfitting Analysis: MLR, ADA, and KNN exhibited the smallest differences between in-sample and out-of-sample performance (Supplementary Figure 1).

Given its strong performance across all criteria, MLR is selected for further machine learning efforts.

The most important features for predicting κ and c_{1x} are covalency, bond strength, and ionic density. Covalency reflects the degree of electron sharing between atoms. Bond strength captures the influence of short, strong bonds on electronic properties. Ionic density distinguishes between covalent and ionic/metallic materials, being lower in the former and higher in the latter. In general, covalent materials exhibit low κ and c_{1x} values typically ranging from 0.2 to 0.3. For ionic materials, the ML algorithm tends to maximize κ and minimize c_{1x} in an effort to achieve larger bandgaps; however, these are often unattainable due to SCAN's limitations discussed previously for this class of solids.

As observed in Table III, PBE has the highest MAE (1.27 eV) and a relatively high σ (0.96 eV) in bandgap prediction. SCAN improves upon PBE with a lower MAE (0.88 eV) and σ (0.78 eV). SD-SCAN, which involves manually fitting parameters to optimize the bandgap, achieves the lowest MAE (0.32 eV) and σ (0.6 eV), indicating the best performance among the methods and representing the best possible result. Similarly, ML-SCAN performs well with an intermediate MAE (0.60 eV) and σ (0.74 eV). ML-SCAN outperforms PBE and SCAN but does not surpass SD-SCAN, as expected.

The cubic system, containing the most materials, displays the highest MAE and σ across all crystal systems and XC functionals. As observed in Table IV the most significant errors arise from the rocksalt structures, which exhibit the highest MAE and σ among all cubic systems, thereby elevating the overall metrics. This is likely because most rocksalt systems predominantly exhibit ionic bonding, which SCAN struggles to predict accurately for the bandgap. Reparametrization alone cannot fully correct this limitation.

While direct comparisons with other ML-based bandgap studies are limited by dataset overlap, the proposed approach shows comparable accuracy. It outperforms Nagai et al. [45], whose model wasn't tailored for bandgap prediction (Supplementary Table 5), and performs similarly to Lui et al. [43] (Supplementary Table 6). Lentz et al. [42] achieve better results, likely due to their focused training on just seven materials with dopants and temperature effects (Supplementary Table 7). Borlido et al. [33] also report a lower MAE (0.45 eV), but their model uses more descriptors and multiple XC functionals, increasing computational cost. Overall, this study delivers competitive performance within the scope of its materials and methods.

To benchmark ML-SCAN, a small set of materials was tested with G_0W_0 and HSE06 (Supplementary Table 1). While ML-SCAN doesn't outperform these methods, it achieves comparable accuracy at a much lower computational cost. Bandgap relative errors were 16% (G_0W_0), 12% (HSE06), and 18% (ML-SCAN); corresponding MAEs were 0.34, 0.52, and 0.76 eV. Despite the limited sample size, the results indicate that ML-SCAN balances accuracy and efficiency, making it a strong candidate for large-scale or resource-constrained studies. Future work could further refine its performance and broaden validation, potentially narrowing the gap with GW and hybrid functionals.

TABLE III. Mean absolute error (standard deviation) using PBE, SCAN, SD-SCAN, SCAN-0.2, and ML-SCAN in predicting the bandgap (eV) of various semiconductors and insulators classified by crystal system (CS). ML-SCAN values correspond to the leave-one-out cross-validation (LOOCV) out-of-sample accuracy of the multiple linear regression (MLR) algorithm.

CS	Materials	PBE	SCAN	SD-SCAN	SCAN-0.2	ML-SCAN
Cubic	104	1.56 (1.18)	1.14 (0.96)	0.47 (0.76)	0.92 (0.92)	0.85 (0.98)
Hexagonal	26	1.10 (0.72)	0.75 (0.54)	0.16 (0.34)	0.43 (0.42)	0.37 (0.42)
Monoclinic	4	1.50 (0.71)	1.00 (0.60)	0.50 (0.57)	0.75 (0.50)	0.80 (0.50)
Orthorhombic	11	0.73 (0.64)	0.47 (0.45)	0.13 (0.26)	0.31 (0.36)	0.31 (0.30)
Tetragonal	87	1.08 (0.73)	0.73 (0.60)	0.23 (0.51)	0.46 (0.51)	0.44 (0.50)
Trigonal	28	1.10 (0.72)	0.67 (0.51)	0.23 (0.34)	0.48 (0.31)	0.47 (0.33)
TOTAL	260	1.27 (0.96)	0.88 (0.78)	0.32 (0.60)	0.64 (0.71)	0.60 (0.74)

TABLE IV. Mean absolute error (standard deviation) using PBE, SCAN, SD-SCAN, SCAN-0.2, and ML-SCAN in predicting the bandgap (eV) of various cubic semiconductors and insulators subclassified by crystal system (CS). ML-SCAN values correspond to the leave-one-out cross-validation (LOOCV) out-of-sample accuracy of the multiple linear regression (MLR) algorithm.

CS	Materials	PBE	SCAN	SD-SCAN	SCAN-0.2	ML-SCAN
Diamond	5	0.99 (0.35)	0.63 (0.19)	0.08 (0.17)	0.50 (0.52)	0.46 (0.41)
Rocksalt	52	2.06 (1.38)	1.57 (1.12)	0.76 (0.94)	1.35 (1.05)	1.27 (1.17)
Zinc-blende	31	1.06 (0.63)	0.71 (0.51)	0.12 (0.28)	0.37 (0.46)	0.32 (0.39)
CsCl	9	1.17 (0.91)	0.84 (0.66)	0.38 (0.53)	0.64 (0.52)	0.60 (0.59)
Others	7	0.93 (0.48)	0.63 (0.47)	0.28 (0.47)	0.80 (0.39)	0.65 (0.49)
TOTAL	104	1.56 (1.18)	1.14 (0.96)	0.47 (0.76)	0.92 (0.92)	0.85 (0.98)

SCAN-0.2: Given that the electronic behavior of semiconductors and insulators is more accurately captured with a lower value of c_{1x}, this effect was tested on the dataset of 260 materials. The SCAN-0.2 functional was constructed by fixing $c_{1x} = 0.2$ while keeping all other SCAN parameters unchanged. This approach is conceptually similar to PBEsol, which improves predictions for solids and surfaces by adjusting specific PBE parameters. Similarly, SCAN-0.2 improves bandgap predictions by reducing c_{1x}, thereby producing a more gradual screening of the exchange interaction across regions of varying electron density.

As observed in Table III, SCAN-0.2 shows good performance, with an intermediate MAE (0.64 eV) and standard deviation (0.71 eV). It shows a notable improvement over standard SCAN across all crystal systems and achieves accuracy comparable to ML-SCAN, making it well-suited for modeling semiconductors and insulators.

While ML-SCAN generally performs slightly better, such as in carbon, where it predicts a bandgap of 4.25 eV compared to 4.02 eV from SCAN-0.2, there are exceptions. For instance, in monoclinic systems, SCAN-0.2 shows superior results. Overall, ML-SCAN outperforms SCAN-0.2 on 58% of the materials studied, whereas SCAN-0.2 outperforms ML-SCAN on the remaining 42%.

Regarding structural predictions for the materials in Table I (excluding noble gases), SCAN underestimates lattice parameters by approximately -0.2%, while SCAN-0.2 increases this to -0.4%. However, the average deviation remains small (0.02 Å) and is considered negligible (Supplementary Table 13).

III. DISCUSSION

This work presents a system-dependent XC functional, SD-SCAN, created by fitting internal SCAN parameters to improve the prediction of electronic band gaps in semiconductors and insulators. Acceptable adjustment ranges were identified to preserve physical plausibility while improving the accuracy of bandgaps and related properties. The proposed SD-SCAN functional enhances the description of covalent materials by more accurately capturing the conduction band edge and associated charge distributions. However, for highly ionic compounds, the experimental bandgaps remain inaccessible due to the absence of long-range exchange and limitations of the SCAN functional.

By employing machine learning, specifically the ML-SCAN model, this study demonstrates that SCAN's internal parameters can be systematically related to material properties, highlighting the potential of data-driven approaches in functional design. Additionally, a simplified adjustment, SCAN-0.2 (with $c_{1x} = 0.2$), offers an effective shortcut for improving bandgap predictions in a wide range of semiconductors and insulators.

This work represents a first step toward developing a system-dependent XC functional specifically for semiconductors and insulators. Future research should explore new adaptive, ML-driven XC functionals capable of accurately describing the electronic properties of these materials. Such advancements will enable the accurate prediction of other physical properties, such as band alignment and solar cell efficiency.

IV. METHODS

A. DFT calculations

The materials in this study are analyzed using Density Functional Theory [72], with exchange and correlation effects addressed via LDA [7–9], PBE [10], SCAN [11], and SD-SCAN functionals. Valence electron wave functions are described using the projector augmented-wave (PAW) method [73]. A Γ-centered k-point mesh, following the Monkhorst-Pack scheme [74], samples the irreducible Brillouin zone for each structure. Total energy optimization within each cell achieves a maximum error of 1 meV/atom, and self-consistent solutions of the KS equations ensure a total energy difference of less than 10^{-6} eV. Calculations are performed using the Vienna Ab Initio Simulation Package (VASP) [75, 76], with internal modifications for the SD-SCAN XC functional to directly read SCAN parameters from the INCAR file.

B. G_0W_0 calculations

Quasiparticle bandgaps are obtained from one-shot G_0W_0@PBE calculations using VASP. For each semiconductor, we start from a converged PBE ground state (with the same preconverged cutoff and k-point mesh), compute additional unoccupied states, and then perform a one-shot G_0W_0 step to obtain the bandgaps.

C. Hybrid HSE06 calculations

HSE06 bandgaps were computed using 25% short-range exact exchange and a screening parameter of 0.2. Structures were first relaxed with HSE06, and a subsequent self-consistent calculation on the relaxed geometry was used to obtain the final band edges.

D. Machine learning models for SCAN parameters

Supervised machine learning regression algorithms to predict κ and c_{1x} XC parameters. The MLR model includes an intercept and uses the ordinary least squares loss function. The KNN algorithm is optimized with four neighbors. The DT Regressor uses a fixed random seed (random state=42) and imposes no explicit tree-depth constraint. The RF model has 100 estimators and a fixed random seed (random state=42) with default parameters, including unlimited tree depth. The ADA model uses 50 estimators, a fixed random seed (random state=42), and the default DecisionTree with a maximum depth of 3, a learning rate of 1.0, and a linear loss function. The GBR model is configured with 100 estimators, a fixed random seed (random state=0), and default settings, including a squared error loss function and a learning rate of 0.1. All other parameters use default values.

ADDITIONAL INFORMATION

This section provides additional references for experimental data that were utilized in training the machine learning algorithms but are not explicitly discussed in the main text [77–177]. Further details on each citation can be found in Supplementary Table 8.

CODE AND DATA AVAILABILITY

Datasets, scripts, and resources related to this work are available at: https://github.com/vdovale29/SD-SCAN.git and https://github.com/usnistgov/chips-SD-SCAN.git.

AUTHOR CONTRIBUTIONS

V.D.F. conceived the study, performed the calculations, and wrote the main manuscript. P.T. modified the SCAN code to enable SD-SCAN calculations. M.A.L.M. contributed to the theoretical framework, provided the database of experimental bandgaps used in this study, and critically revised the manuscript. S.D. guided the statistical analysis of the machine learning model and contributed to the interpretation of the machine learning results. K.C. and A.B.H. contributed to the interpretation of results and critical revision of the manuscript. A.H.R. supervised the study and provided scientific guidance throughout the project and during manuscript preparation. All authors (V.D.F., P.T., M.A.L.M., S.D., K.C., A.B.H., and A.H.R.) read and approved the final version of the manuscript.

COMPETING INTERESTS

The authors do not declare any Competing Financial or Non-Financial Interests. Kamal Choudhary is an Editor of *npj Computational Materials*.

ACKNOWLEDGMENTS

We thank the Pittsburgh Supercomputer Center (Bridges2) and the San Diego Supercomputer Center (Expanse) for allocation DMR140031 from the Advanced Cyberinfrastructure Coordination Ecosystem: Services & Support (ACCESS) program, which is supported by the National Science Foundation grants #2138259, #2138286, #2138307, #2137603, and #2138296. We also recognize the computational resources provided by

the WVU Research Computing Dolly Sods HPC cluster, which is funded in part by NSF OAC-2117575. We also acknowledge support from the West Virginia Higher Education Policy Commission under the Research Challenge Grant Program 2022 (Award RCG 23-007) and the NASA EPSCoR Award 80NSSC22M0173. K.C. thanks funding from the CHIPS Metrology Program, part of CHIPS for America, National Institute of Standards and Technology, U.S. Department of Commerce. Certain commercial equipment, instruments, software, or materials are identified in this paper to ensure adequate specification of the experimental procedure. Such identifications are not intended to imply recommendation or endorsement by NIST, nor are they intended to imply that the materials or equipment identified are necessarily the best available for the purpose.

[1] C. Kittel, *Introduction to solid state physics* (John Wiley & Sons, 2018).
[2] W. D. Callister Jr and D. G. Rethwisch, *Fundamentals of materials science and engineering: an integrated approach* (John Wiley & Sons, 2020).
[3] A. Al-Azzawi, *Light and optics: principles and practices* (CRC Press, 2018).
[4] F. J. DiSalvo, Thermoelectric cooling and power generation, Science **285**, 703 (1999).
[5] F. Giustino, *Materials modelling using density functional theory: properties and predictions* (Oxford University Press, 2014).
[6] J. G. Lee, *Computational Materials Science: An Introduction* (CRC press, 2016).
[7] D. M. Ceperley and B. J. Alder, Ground state of the electron gas by a stochastic method, Physical review letters **45**, 566 (1980).
[8] P. A. Dirac, Note on exchange phenomena in the Thomas atom, in *Mathematical proceedings of the Cambridge philosophical society*, Vol. 26 (Cambridge University Press, 1930) pp. 376–385.
[9] J. P. Perdew and A. Zunger, Self-interaction correction to density-functional approximations for many-electron systems, Physical review B **23**, 5048 (1981).
[10] J. P. Perdew, K. Burke, and M. Ernzerhof, Generalized gradient approximation made simple, Physical review letters **77**, 3865 (1996).
[11] J. Sun, A. Ruzsinszky, and J. P. Perdew, Strongly constrained and appropriately normed semilocal density functional, Physical review letters **115**, 036402 (2015).
[12] J. Heyd, G. E. Scuseria, and M. Ernzerhof, Hybrid functionals based on a screened coulomb potential, The Journal of chemical physics **118**, 8207 (2003).
[13] J. Heyd and G. E. Scuseria, Efficient hybrid density functional calculations in solids: Assessment of the heyd–scuseria–ernzerhof screened coulomb hybrid functional, The Journal of chemical physics **121**, 1187 (2004).
[14] J. Heyd, G. E. Scuseria, and M. Ernzerhof, Erratum: "hybrid functionals based on a screened coulomb potential" [j. chem. phys. 118, 8207 (2003)], The Journal of chemical physics **124**, 219906 (2006).
[15] A. V. Krukau, O. A. Vydrov, A. F. Izmaylov, and G. E. Scuseria, Influence of the exchange screening parameter on the performance of screened hybrid functionals, The Journal of chemical physics **125** (2006).
[16] M. Shishkin and G. Kresse, Implementation and performance of the frequency-dependent gw method within the paw framework, Physical Review B—Condensed Matter and Materials Physics **74**, 035101 (2006).
[17] M. Shishkin and G. Kresse, Self-consistent gw calculations for semiconductors and insulators, Physical Review B—Condensed Matter and Materials Physics **75**, 235102 (2007).
[18] M. Shishkin, M. Marsman, and G. Kresse, Accurate quasiparticle spectra from self-consistent gw calculations with vertex corrections, Physical review letters **99**, 246403 (2007).
[19] F. Fuchs, J. Furthmüller, F. Bechstedt, M. Shishkin, and G. Kresse, Quasiparticle band structure based on a generalized kohn-sham scheme, Physical Review B—Condensed Matter and Materials Physics **76**, 115109 (2007).
[20] K. Choudhary, Q. Zhang, A. C. Reid, S. Chowdhury, N. Van Nguyen, Z. Trautt, M. W. Newrock, F. Y. Congo, and F. Tavazza, Computational screening of high-performance optoelectronic materials using OptB88vdW and TB-mBJ formalisms, Scientific data **5**, 1 (2018).
[21] J. Klimeš, D. R. Bowler, and A. Michaelides, Chemical accuracy for the van der waals density functional, Journal of Physics: Condensed Matter **22**, 022201 (2009).
[22] H. Peng, Z.-H. Yang, J. Sun, and J. P. Perdew, Scan+ rvv10: A promising van der waals density functional, arXiv preprint arXiv:1510.05712 (2015).
[23] J. Brandenburg, J. Bates, J. Sun, and J. Perdew, Benchmark tests of a strongly constrained semilocal functional with a long-range dispersion correction, Physical Review B **94**, 115144 (2016).
[24] J. P. Perdew, R. G. Parr, M. Levy, and J. L. Balduz Jr, Density-functional theory for fractional particle number: derivative discontinuities of the energy, Physical Review Letters **49**, 1691 (1982).
[25] A. Seidl, A. Görling, P. Vogl, J. A. Majewski, and M. Levy, Generalized kohn-sham schemes and the band-gap problem, Physical Review B **53**, 3764 (1996).
[26] M. Grüning, A. Marini, and A. Rubio, Density functionals from many-body perturbation theory: The band gap for semiconductors and insulators, The Journal of chemical physics **124** (2006).
[27] M. Grüning, A. Marini, and A. Rubio, Effect of spatial nonlocality on the density functional band gap, Physical Review B—Condensed Matter and Materials Physics **74**, 161103 (2006).
[28] J. P. Perdew, W. Yang, K. Burke, Z. Yang, E. K. Gross, M. Scheffler, G. E. Scuseria, T. M. Henderson, I. Y. Zhang, A. Ruzsinszky, *et al.*, Understanding band gaps of solids in generalized Kohn–Sham theory, Proceedings of the national academy of sciences **114**, 2801 (2017).
[29] T. Lebeda, T. Aschebrock, J. Sun, L. Leppert, and S. Kümmel, Right band gaps for the right reason at low

computational cost with a meta-gga, Physical Review Materials **7**, 093803 (2023).
[30] E. E. Salpeter and H. A. Bethe, A relativistic equation for bound-state problems, Physical Review **84**, 1232 (1951).
[31] F. Tran and P. Blaha, Accurate band gaps of semiconductors and insulators with a semilocal exchange-correlation potential, Physical review letters **102**, 226401 (2009).
[32] T. Aschebrock and S. Kümmel, Ultranonlocality and accurate band gaps from a meta-generalized gradient approximation, Physical Review Research **1**, 033082 (2019).
[33] P. Borlido, J. Schmidt, A. W. Huran, F. Tran, M. A. Marques, and S. Botti, Exchange-correlation functionals for band gaps of solids: benchmark, reparametrization and machine learning, npj Computational Materials **6**, 1 (2020).
[34] P. Kovács, P. Blaha, and G. K. Madsen, Origin of the success of mGGAs for bandgaps, The Journal of Chemical Physics **159** (2023).
[35] T. Lebeda, T. Aschebrock, and S. Kümmel, Balancing the contributions to the gradient expansion: Accurate binding and band gaps with a nonempirical meta-gga, Physical Review Letters **133**, 136402 (2024).
[36] T. Lebeda and S. Kümmel, Meta-gga that describes weak interactions in addition to bond energies and band gaps, Physical Review B **111**, 155133 (2025).
[37] D. Wing, G. Ohad, J. B. Haber, M. R. Filip, S. E. Gant, J. B. Neaton, and L. Kronik, Band gaps of crystalline solids from wannier-localization–based optimal tuning of a screened range-separated hybrid functional, Proceedings of the National Academy of Sciences **118**, e2104556118 (2021).
[38] A. J. Garza and G. E. Scuseria, Predicting band gaps with hybrid density functionals, The journal of physical chemistry letters **7**, 4165 (2016).
[39] T. M. Henderson, J. Paier, and G. E. Scuseria, Accurate treatment of solids with the hse screened hybrid, physica status solidi (b) **248**, 767 (2011).
[40] M. A. Marques, M. J. Oliveira, and T. Burnus, Libxc: A library of exchange and correlation functionals for density functional theory, Computer physics communications **183**, 2272 (2012).
[41] S. Lehtola, C. Steigemann, M. J. Oliveira, and M. A. Marques, Recent developments in libxc—a comprehensive library of functionals for density functional theory, SoftwareX **7**, 1 (2018).
[42] L. C. Lentz and A. M. Kolpak, Predicting hse band gaps from pbe charge densities via neural network functionals, Journal of Physics: Condensed Matter **32**, 155901 (2020).
[43] M. Liu, A. Gopakumar, V. I. Hegde, J. He, and C. Wolverton, High-throughput hybrid-functional dft calculations of bandgaps and formation energies and multifidelity learning with uncertainty quantification, Physical Review Materials **8**, 043803 (2024).
[44] K. Pokharel, J. W. Furness, Y. Yao, V. Blum, T. J. Irons, A. M. Teale, and J. Sun, Exact constraints and appropriate norms in machine-learned exchange-correlation functionals, The Journal of Chemical Physics **157** (2022).
[45] R. Nagai, R. Akashi, and O. Sugino, Machine-learning-based exchange correlation functional with physical asymptotic constraints, Physical Review Research **4**, 013106 (2022).
[46] K. Bystrom and B. Kozinsky, Nonlocal machine-learned exchange functional for molecules and solids, Physical Review B **110**, 075130 (2024).
[47] A. Merchant, S. Batzner, S. S. Schoenholz, M. Aykol, G. Cheon, and E. D. Cubuk, Scaling deep learning for materials discovery, Nature **624**, 80 (2023).
[48] J. Schmidt, T. F. Cerqueira, A. H. Romero, A. Loew, F. Jäger, H.-C. Wang, S. Botti, and M. A. Marques, Improving machine-learning models in materials science through large datasets, Materials Today Physics **48**, 101560 (2024).
[49] S. Bernstorff and V. Saile, Experimental determination of band gaps in rare gas solids, Optics communications **58**, 181 (1986).
[50] S. Kim, M. Lee, C. Hong, Y. Yoon, H. An, D. Lee, W. Jeong, D. Yoo, Y. Kang, Y. Youn, *et al.*, A band-gap database for semiconducting inorganic materials calculated with hybrid functional, Scientific Data **7**, 387 (2020).
[51] R. J. Guerrero-Moreno and N. Takeuchi, First principles calculations of the ground-state properties and structural phase transformation in CdO, Physical Review B **66**, 205205 (2002).
[52] F. Tran, P. Blaha, and K. Schwarz, Band gap calculations with becke–johnson exchange potential, Journal of Physics: Condensed Matter **19**, 196208 (2007).
[53] Z.-h. Yang, H. Peng, J. Sun, and J. P. Perdew, More realistic band gaps from meta-generalized gradient approximations: Only in a generalized kohn-sham scheme, Physical review B **93**, 205205 (2016).
[54] D. Evans, A. G. McGlynn, B. M. Towlson, M. Gunn, D. Jones, T. E. Jenkins, R. Winter, and N. R. Poolton, Determination of the optical band-gap energy of cubic and hexagonal boron nitride using luminescence excitation spectroscopy, Journal of Physics: Condensed Matter **20**, 075233 (2008).
[55] G. J. McIntyre, L. Mélési, M. Guthrie, C. Tulk, J. Xu, and J. Parise, One picture says it all—high-pressure cells for neutron Laue diffraction on VIVALDI, Journal of Physics: Condensed Matter **17**, S3017 (2005).
[56] V. Petkov, M. Gateshki, J. Choi, E. Gillan, and Y. Ren, Structure of nanocrystalline GaN from x-ray diffraction, rietveld and atomic pair distribution function analyses, Journal of Materials Chemistry **15**, 4654 (2005).
[57] K. Kam and B. Parkinson, Detailed photocurrent spectroscopy of the semiconducting group VIB transition metal dichalcogenides, The Journal of Physical Chemistry **86**, 463 (1982).
[58] V. Petkov, S. Billinge, P. Larson, S. Mahanti, T. Vogt, K. Rangan, and M. G. Kanatzidis, Structure of nanocrystalline materials using atomic pair distribution function analysis: Study of $LiMoS_2$, Physical Review B **65**, 092105 (2002).
[59] O. O. Kurakevych and V. L. Solozhenko, Rhombohedral boron subnitride, $B_{13}N_2$, by X-ray powder diffraction, Acta Crystallographica Section C: Crystal Structure Communications **63**, i80 (2007).
[60] P. Kovács, F. Tran, P. Blaha, and G. K. Madsen, What is the optimal mgga exchange functional for solids, The Journal of Chemical Physics **157** (2022).
[61] S. Bi, C. Carbogno, I. Y. Zhang, and M. Scheffler, Self-interaction corrected scan functional for molecules and

solids in the numeric atom-center orbital framework, The Journal of Chemical Physics **160** (2024).
[62] P. Verma and D. G. Truhlar, Hle17: An improved local exchange–correlation functional for computing semiconductor band gaps and molecular excitation energies, The Journal of Physical Chemistry C **121**, 7144 (2017).
[63] U. Herath, P. Tavadze, X. He, E. Bousquet, S. Singh, F. Muñoz, and A. H. Romero, Pyprocar: A Python library for electronic structure pre/post-processing, Computer Physics Communications **251**, 107080 (2020).
[64] L. Lang, P. Tavadze, A. Tellez, E. Bousquet, H. Xu, F. Muñoz, N. Vasquez, U. Herath, and A. H. Romero, Expanding PyProcar for new features, maintainability, and reliability, Computer Physics Communications **297**, 109063 (2024).
[65] K. Momma and F. Izumi, *VESTA3* for three-dimensional visualization of crystal, volumetric and morphology data, Journal of Applied Crystallography **44**, 1272 (2011).
[66] S. H. Wemple and M. DiDomenico Jr, Behavior of the electronic dielectric constant in covalent and ionic materials, Physical Review B **3**, 1338 (1971).
[67] A. Dal Corso, S. Baroni, and R. Resta, Density-functional theory of the dielectric constant: Gradient-corrected calculation for silicon, Physical Review B **49**, 5323 (1994).
[68] G. Onida, L. Reining, and A. Rubio, Electronic excitations: density-functional versus many-body green's-function approaches, Reviews of modern physics **74**, 601 (2002).
[69] S. Botti, A. Schindlmayr, R. Del Sole, and L. Reining, Time-dependent density-functional theory for extended systems, Reports on Progress in Physics **70**, 357 (2007).
[70] A. Tal, P. Liu, G. Kresse, and A. Pasquarello, Accurate optical spectra through time-dependent density functional theory based on screening-dependent hybrid functionals, Physical Review Research **2**, 032019 (2020).
[71] D. E. Aspnes and A. Studna, Dielectric functions and optical parameters of Si, Ge, GaP, GaAs, GaSb, InP, InAs, and InSb from 1.5 to 6.0 eV, Physical review B **27**, 985 (1983).
[72] W. Kohn and L. J. Sham, Self-consistent equations including exchange and correlation effects, Physical review **140**, A1133 (1965).
[73] P. E. Blöchl, Projector augmented-wave method, Physical review B **50**, 17953 (1994).
[74] H. J. Monkhorst and J. D. Pack, Special points for Brillouin-zone integrations, Physical review B **13**, 5188 (1976).
[75] G. Kresse and J. Furthmüller, Efficient iterative schemes for ab initio total-energy calculations using a plane-wave basis set, Physical review B **54**, 11169 (1996).
[76] G. Kresse and J. Furthmüller, Efficiency of ab-initio total energy calculations for metals and semiconductors using a plane-wave basis set, Computational materials science **6**, 15 (1996).
[77] O. A. Golikova, N. E. Solovev, Y. A. Ugai, and V. A. Feigelman, Electrophysical properties of α-rhombohedral boron, Physica status solidi (a) **86**, K51 (1984).
[78] M. Feneberg, R. A. Leute, B. Neuschl, K. Thonke, and M. Bickermann, High-excitation and high-resolution photoluminescence spectra of bulk AlN, Physical Review B **82**, 075208 (2010).
[79] H. A. Al-Brithen, A. R. Smith, and D. Gall, Surface and bulk electronic structure of ScN (001) investigated by scanning tunneling microscopy/spectroscopy and optical absorption spectroscopy, Physical Review B **70**, 045303 (2004).
[80] P. P. Altermatt, T. Kiesewetter, K. Ellmer, and H. Tributsch, Specifying targets of future research in photovoltaic devices containing pyrite (FeS_2) by numerical modelling, Solar energy materials and solar cells **71**, 181 (2002).
[81] G. Ambrazevičius, G. Babonas, Y. V. Rud, and A. Šileika, The fundamental absorption edge of $MgSiP_2$, physica status solidi (b) **106**, 85 (1981).
[82] D. Baer and D. L. Blanchard Jr, Studies of the calcite cleavage surface for comparison with calculation, Applied surface science **72**, 295 (1993).
[83] G. Baldini and B. Bosacchi, Optical properties of Na and Li halide crystals at 55 K, physica status solidi (b) **38**, 325 (1970).
[84] G. Boda, B. Stenström, V. Sagredo, O. Beckman, B. Carlsson, and S. Rundqvist, Magnetic and electric properties of FeP_2 single crystals, Physica Scripta **4**, 132 (1971).
[85] M. Bost and J. E. Mahan, An investigation of the optical constants and band gap of chromium disilicide, Journal of Applied Physics **63**, 839 (1988).
[86] S. Broadley, Z. A. Gál, F. Corà, C. F. Smura, and S. J. Clarke, Vertex-linked ZnO_2S_2 tetrahedra in the oxysulfide BaZnOS: a new coordination environment for zinc in a condensed solid, Inorganic Chemistry **44**, 9092 (2005).
[87] D. E. Bugaris, C. D. Malliakas, D. P. Shoemaker, D. T. Do, D. Y. Chung, S. D. Mahanti, and M. G. Kanatzidis, Crystal growth and characterization of the narrow-band-gap semiconductors $OsPn_2$ (Pn = P, As, Sb), Inorganic Chemistry **53**, 9959 (2014).
[88] L. A. Burton, T. J. Whittles, D. Hesp, W. M. Linhart, J. M. Skelton, B. Hou, R. F. Webster, *et al.*, Electronic and optical properties of single crystal SnS_2: An earth-abundant disulfide photocatalyst, Journal of Materials Chemistry A **4**, 1312 (2016).
[89] H. Chen, P.-F. Liu, B.-X. Li, H. Lin, L.-M. Wu, and X.-T. Wu, Experimental and theoretical studies on the NLO properties of two quaternary non-centrosymmetric chalcogenides: $BaAg_2GeS_4$ and $BaAg_2SnS_4$, Dalton Transactions **47**, 429 (2018).
[90] A. Conan, D. Delaunay, A. Bonnet, A. Moustafa, and M. Spiesser, Temperature dependence of the electrical conductivity and thermoelectric power in $MoTe_2$ single crystals, physica status solidi (b) **94**, 279 (1979).
[91] J. D. Denlinger, J. A. Clack, J. W. Allen, G.-H. Gweon, D. M. Poirier, C. G. Olson, J. L. Sarrao, A. D. Bianchi, and Z. Fisk, Bulk band gaps in divalent hexaborides, Physical review letters **89**, 157601 (2002).
[92] J. W. Fleming, M. J. Weber, G. W. Day, A. Feldman, B. H. Chai, M. G. Kuzyk, W. R. Holland, *et al.*, *Handbook of Optical Materials* (CRC Press, 2018).
[93] R. H. French, Electronic band structure of Al_2O_3, with comparison to Alon and AlN, Journal of the American Ceramic Society **73**, 477 (1990).
[94] D. Fröhlich and B. Staginnus, New assignment of the band gap in the alkali bromides by two-photon spectroscopy, Physical Review Letters **19**, 496 (1967).

[95] F. Gäbler, M. Kirchner, W. Schnelle, U. Schwarz, M. Schmitt, H. Rosner, and R. Niewa, $(Sr_3N)E$ and $(Ba_3N)E$ (E=Sb,Bi): Synthesis, crystal structures, and physical properties, Zeitschrift für anorganische und allgemeine Chemie **630**, 2292 (2004).

[96] S. Glaus and G. Calzaferri, The band structures of the silver halides AgF, AgCl, and AgBr: A comparative study, Photochemical & Photobiological Sciences **2**, 398 (2003).

[97] D. L. Greenaway and R. Nitsche, Preparation and optical properties of group IV–VI2 chalcogenides having the CdI_2 structure, Journal of Physics and Chemistry of Solids **26**, 1445 (1965).

[98] T. R. Griffiths and J. Dixon, Electron irradiation of single crystal thorium dioxide and electron transfer reactions, Inorganica Chimica Acta **300**, 305 (2000).

[99] C. Ho and S. Lin, Optical properties of the interband transitions of layered gallium sulfide, Journal of applied physics **100** (2006).

[100] W. Honeyman and K. Wilkinson, Growth and properties of single crystals of group I-III-VI2 ternary semiconductors, Journal of Physics D: Applied Physics **4**, 1182 (1971).

[101] J. Huang, Y. Huang, and T.-R. Yang, An optical absorption study of RuS_2 single crystals, Journal of Physics: Condensed Matter **7**, 4175 (1995).

[102] G. R. Huggett and K. Teegarden, Intrinsic photoconductivity in the alkali halides, Physical Review **141**, 797 (1966).

[103] L. Isaenko, P. Krinitsin, V. Vedenyapin, A. Yelisseyev, A. Merkulov, J.-J. Zondy, and V. Petrov, $LiGaTe_2$: A new highly nonlinear chalcopyrite optical crystal for the Mid-IR, Crystal Growth & Design **5**, 1325 (2005).

[104] G. E. Jellison Jr, I. E. Paulauskas, L. A. Boatner, and D. J. Singh, Optical properties and band structure of $KTaO_3$, Physical Review B **74** (2006).

[105] M.-S. Jin and W.-T. Kim, Blue photoluminescence of $CdAl_2S_4$ single crystal, Applied Physics Letters **70**, 484 (1997).

[106] B. S. Joo, Y. J. Chang, L. Moreschini, A. Bostwick, E. Rotenberg, and M. Han, Evidence for indirect band gap in $BaSnO_3$ using angle-resolved photoemission spectroscopy, Current Applied Physics **17**, 595 (2017).

[107] T. Kajiki, Y. Hayashi, and H. Takizawa, High-pressure synthesis of a new copper thioborate, $CuBS_2$, Materials Letters **61**, 2382 (2007).

[108] A. Kaltzoglou, M. Antoniadou, A. G. Kontos, C. C. Stoumpos, D. Perganti, E. Siranidi, V. Raptis, K. Trohidou, V. Psycharis, M. G. Kanatzidis, and P. Falaras, Optical-vibrational properties of the Cs_2SnX_6 (X = Cl, Br, I) defect perovskites and hole-transport efficiency in dye-sensitized solar cells, The Journal of Physical Chemistry C **120**, 11777 (2016).

[109] K. K. Kam and B. A. Parkinson, Detailed photocurrent spectroscopy of the semiconducting group VIB transition metal dichalcogenides, The Journal of Physical Chemistry **86**, 463 (1982).

[110] Y. Kaneko and T. Koda, New developments in IIa–VIb (alkaline-earth chalcogenide) binary semiconductors, Journal of Crystal Growth **86**, 72 (1988).

[111] K. Kayanuma, R. Kawamura, H. Hiramatsu, H. Yanagi, M. Hirano, T. Kamiya, and H. Hosono, Heteroepitaxial growth of layered semiconductors, LaZnOPn (Pn= P and As), Thin Solid Films **516**, 5800 (2008).

[112] Y.-I. Kim and P. M. Woodward, Crystal structures and dielectric properties of ordered double perovskites containing Mg^{2+} and Ta^{5+}, Journal of Solid State Chemistry **180**, 2798 (2007).

[113] S.-i. Kimura, F. Arai, and M. Ikezawa, Optical study on electronic structure of rare-earth sesquioxides, Journal of the Physical Society of Japan **69**, 3451 (2000).

[114] L. A. Koscielski, E. Ringe, R. P. Van Duyne, D. E. Ellis, and J. A. Ibers, Single-crystal structures, optical absorptions, and electronic distributions of thorium oxychalcogenides ThOQ (Q = S, Se, Te), Inorganic Chemistry **51**, 8112 (2012).

[115] A. Kudo, H. Yanagi, H. Hosono, and H. Kawazoe, $SrCu_2O_2$: A p-type conductive oxide with wide band gap, Applied Physics Letters **73**, 220 (1998).

[116] O. V. Kulikova, N. A. Moldovyan, S. M. Popov, S. I. Radautsan, and A. V. Siminel, Optical absorption and Raman scattering of spinel type semiconductor $ZnAl_2S_4$, Japanese Journal of Applied Physics **32**, 586 (1993).

[117] K. Kuriyama and T. Katoh, Optical band gap of the filled tetrahedral semiconductor LiZnP, Physical Review B **37**, 7140 (1988).

[118] K. Kuriyama, T. Kato, and K. Kawada, Optical band gap of the filled tetrahedral semiconductor LiZnAs, Physical Review B **49**, 11452 (1994).

[119] K. Kuriyama, R. Taguchi, K. Kushida, and K. Ushiyama, Growth and band gap of the filled tetrahedral semiconductor LiZnN, Journal of crystal growth **198**, 802 (1999).

[120] K. Kushida and K. Kuriyama, Narrowing of the Co-3d band related to the order–disorder phase transition in $LiCoO_2$, Solid state communications **123**, 349 (2002).

[121] P. Kushwaha, A. Patra, E. Anjali, H. Surdi, A. Singh, C. Gurada, S. Ramakrishnan, S. Prabhu, A. V. Gopal, and A. Thamizhavel, Physical, optical and nonlinear properties of InS single crystal, Optical Materials **36**, 616 (2014).

[122] J. W. Lekse, M. K. Underwood, J. P. Lewis, and C. Matranga, Synthesis, characterization, electronic structure, and photocatalytic behavior of $CuGaO_2$ and $CuGa_{1-x}Fe_xO_2$ ($x = 0.05, 0.10, 0.15, 0.20$) delafossites, The Journal of Physical Chemistry C **116**, 1865 (2012).

[123] S. Levcenco, D. Dumcenco, Y.-S. Huang, E. Arushanov, V. Tezlevan, K.-K. Tiong, and C. Du, Near band edge anisotropic optical transitions in wide band gap semiconductor Cu_2ZnSiS_4, Journal of Applied Physics **108** (2010).

[124] F. Liang, L. Kang, Z. Lin, and Y. Wu, Mid-infrared nonlinear optical materials based on metal chalcogenides: Structure–property relationship, Crystal Growth & Design **17**, 2254 (2017).

[125] P. Liao, J. Huang, Y. Huang, and T.-R. Yang, An optical-absorption study of $RuTe_2$ single crystals, Solid state communications **98**, 279 (1996).

[126] X. Liu, K. Matsuda, Y. Moritomo, A. Nakamura, and N. Kojima, Electronic structure of the gold complexes $Cs_2Au_2X_6$ (X= I, Br, and Cl), Physical Review B **59**, 7925 (1999).

[127] M. L. Liu, L. B. Wu, F. Q. Huang, L. D. Chen, and J. A. Ibers, Syntheses, crystal and electronic structure, and some optical and transport properties of LnCuOTe (Ln= La, Ce, Nd), Journal of Solid State Chemistry **180**, 62 (2007).

[128] O. Madelung, *Semiconductors: Data Handbook* (Springer Science & Business Media, 2004).

[129] F. E. Martin and E. B. Hensley, Photoelectric emission from barium telluride, Physical Review **163**, 219 (1967).

[130] H. Matsushita, T. Maeda, A. Katsui, and T. Takizawa, Thermal analysis and synthesis from the melts of cu-based quaternary compounds Cu–III–IV–VI4 and Cu_2–II–IV–VI4 (II= Zn, Cd; III= Ga, In; IV= Ge, Sn; VI= Se), Journal of crystal growth **208**, 416 (2000).

[131] J. McLeod, R. Wilks, N. Skorikov, L. Finkelstein, M. Abu-Samak, E. Kurmaev, and A. Moewes, Band gaps and electronic structure of alkaline-earth and post-transition-metal oxides, Physical Review B **81**, 245123 (2010).

[132] T. Miyata and T. Tomiki, Optical studies of NaCl single crystals in 10 eV region II. the spectra of conductivity at low temperatures, absorption constant and energy loss, Journal of the Physical Society of Japan **24**, 1286 (1968).

[133] M. Miyauchi, Z. Liu, Z.-G. Zhao, S. Anandan, and K. Hara, Single crystalline zinc stannate nanoparticles for efficient photo-electrochemical devices, Chemical Communications **46**, 1529 (2010).

[134] H. Mizoguchi and P. M. Woodward, Electronic structure studies of main group oxides possessing edge-sharing octahedra: Implications for the design of transparent conducting oxides, Chemistry of Materials **16**, 5233 (2004).

[135] M. Moustafa, T. Zandt, C. Janowitz, and R. Manzke, Growth and band gap determination of the ZrS_xSe_{2-x} single crystal series, Physical Review B **80**, 035206 (2009).

[136] R. Nagarajan, N. Duan, M. Jayaraj, J. Li, K. Vanaja, A. Yokochi, A. Draeseke, J. Tate, and A. Sleight, p-type conductivity in the delafossite structure, International Journal of Inorganic Materials **3**, 265 (2001), university of California Santa Barbara Conference papers.

[137] S.-i. Nakai and T. Sagawa, Na^+ $L_{2,3}$ absorption spectra of sodium halides, Journal of the Physical Society of Japan **26**, 1427 (1969).

[138] H. Nakanishi, Fundamental absorption edge in $CdIn_2S_4$, Japanese Journal of Applied Physics **19**, 103 (1980).

[139] H. Nhalil, D. Han, M.-H. Du, S. Chen, D. Antonio, K. Gofryk, and B. Saparov, Optoelectronic properties of candidate photovoltaic Cu_2PbSiS_4, Ag_2PbGeS_4 and KAg_2SbS_4 semiconductors, Journal of Alloys and Compounds **746**, 405 (2018).

[140] J. Oestreich, U. Probst, F. Richardt, and E. Bucher, Thermoelectrical properties of the compounds $ScM^{VIII}Sb$ and $YM^{VIII}Sb$ (M^{VIII} = Ni, Pd, Pt), Journal of Physics: Condensed Matter **15**, 635 (2003).

[141] S. Ouyang, N. Kikugawa, D. Chen, Z. Zou, and J. Ye, A systematical study on photocatalytic properties of $AgMO_2$ (M= Al, Ga, In): Effects of chemical compositions, crystal structures, and electronic structures, The Journal of Physical Chemistry C **113**, 1560 (2009).

[142] S. Ozaki, K.-I. Muto, H. Nagata, and S. Adachi, Optical absorption and emission in the defect-chalcopyrite semiconductor $CdGa_2Te_4$, Journal of applied physics **97** (2005).

[143] C.-H. Park, R. Kykyneshi, A. Yokochi, J. Tate, and D. A. Keszler, Structure and physical properties of BaCuTeF, Journal of Solid State Chemistry **180**, 1672 (2007).

[144] J. Pascual, J. Camassel, and H. Mathieu, Fine structure in the intrinsic absorption edge of TiO_2, Physical Review B **18**, 5606 (1978).

[145] L. Peedikakkandy and P. Bhargava, Composition dependent optical, structural and photoluminescence characteristics of cesium tin halide perovskites, RSC Advances **6**, 19857 (2016).

[146] J. Pellicer-Porres, A. Segura, A. Gilliland, A. Munoz, P. Rodríguez-Hernández, D. Kim, M. Lee, and T. Kim, On the band gap of $CuAlO_2$ delafossite, Applied physics letters **88** (2006).

[147] E. Y. Peresh, V. Sidei, O. Zubaka, and I. Stercho, $K_2(Rb_2,Cs_2,Tl_2)TeBr_6(I_6)$ and $Rb_3(Cs_3)Sb_2(Bi_2)Br_9(I_9)$ perovskite compounds, Inorganic Materials **47**, 208 (2011).

[148] A. Ray, H. M. Smith, and N. M. Haegel, Temperature dependence of the indirect bandgap in thallium bromide from cathodoluminescence spectroscopy, Journal of Applied Physics **115** (2014).

[149] O. Reckeweg, C. Lind, A. Simon, and F. J. DiSalvo, Rietveld refinement of the crystal structure of α-Be_3N_2 and the experimental determination of optical band gaps for Mg_3N_2, Ca_3N_2 and $CaMg_2N_2$, Zeitschrift für Naturforschung B **58**, 159 (2003).

[150] A. Richard, J. Russell, A. Zakutayev, L. Zakharov, D. Keszler, and J. Tate, Synthesis, structure, and optical properties of BiCuOCh (Ch= S, Se, and Te), Journal of Solid State Chemistry **187**, 15 (2012).

[151] D. Roessler and W. Walker, Electronic spectra of crystalline NaCl and KCl, Physical Review **166**, 599 (1968).

[152] G. Rubloff, Far-ultraviolet reflectance spectra and the electronic structure of ionic crystals, Physical review B **5**, 662 (1972).

[153] T. Sambrook, C. F. Smura, S. J. Clarke, K. M. Ok, and P. S. Halasyamani, Structure and physical properties of the polar oxysulfide CaZnOS, Inorganic Chemistry **46**, 2571 (2007).

[154] D. M. Schleich and A. Wold, Optical and electrical properties of quarternary chalcogenides, Materials Research Bulletin **12**, 111 (1977).

[155] M. Schreyer and M. Jansen, Synthesis, structure and properties of Ag_2PdO_2, Solid State Sciences **3**, 25 (2001).

[156] G. A. Slack, T. F. McNelly, and E. Taft, Melt growth and properties of B_6P crystals, Journal of Physics and Chemistry of Solids **44**, 1009 (1983).

[157] C. Sugiura, K-x-ray spectra and electronic band structures of $MgCl_2$, $CaCl_2$, $SrCl_2$, and $BaCl_2$, Physical Review B **9**, 2679 (1974).

[158] A. J. Taylor, R. B. Gibson, and J. P. Roberts, Two-photon absorption at 248 nm in ultraviolet window materials, Optics Letters **13**, 814 (1988).

[159] K. Teegarden and G. Baldini, Optical absorption spectra of the alkali halides at 10 K, Physical Review **155**, 896 (1967).

[160] C. L. Teske, W. Bensch, S. Mankovsky, and H. Ebert, Preparation, crystal structure, physical properties and electronic band structure of $TlScQ_2$ (Q= S, Se and Te), Zeitschrift für anorganische und allgemeine Chemie **634**, 445 (2008).

[161] J. Thomas, G. Stephan, J. Lemonnier, M. Nisar, and S. Robin, Optical anisotropy of MgF, in its UV absorption region, physica status solidi (b) **56**, 163 (1973).

[162] L.-H. Tjeng, M. B. Meinders, J. van Elp, J. Ghijsen, G. A. Sawatzky, and R. L. Johnson, Electronic structure of Ag_2O, Physical Review B **41**, 3190 (1990).

[163] T. M. Tolhurst, C. Braun, T. D. Boyko, W. Schnick, and A. Moewes, Experiment-driven modeling of crystalline phosphorus nitride P_3N_5: Wide-ranging implications from a unique structure, Chemistry–A European Journal **22**, 10475 (2016).

[164] K. Ueda, S. Inoue, H. Hosono, N. Sarukura, and M. Hirano, Room-temperature excitons in wide-gap layered-oxysulfide semiconductor: LaCuOS, Applied Physics Letters **78**, 2333 (2001).

[165] K. Ueda and H. Hosono, Band gap engineering, band edge emission, and p-type conductivity in wide-gap $LaCuOS_{1-x}Se_x$ oxychalcogenides, Journal of Applied Physics **91**, 4768 (2002).

[166] K. Van Benthem, C. Elsässer, and R. French, Bulk electronic structure of $SrTiO_3$: Experiment and theory, Journal of applied physics **90**, 6156 (2001).

[167] H. Vaterlaus, R. Bichsel, F. Levy, and H. Berger, RuS_2 and $RuSe_2$ single crystals: a study of phonons, optical absorption and electronic properties, Journal of Physics C: Solid State Physics **18**, 6063 (1985).

[168] C.-H. Wang, B. J. Kennedy, A. L. Menezes de Oliveira, J. Polt, and K. S. Knight, The impact of anion ordering on octahedra distortion and phase transitions in $SrTaO_2N$ and $BaTaO_2N$, Acta Crystallographica Section B: Structural Science, Crystal Engineering and Materials **73**, 389 (2017).

[169] Y. Wu and W. Bensch, Syntheses, crystal structures and spectroscopic properties of Ag_2Nb $[P_2S_6][S_2]$ and KAg_2 $[PS_4]$, Journal of Solid State Chemistry **182**, 471 (2009).

[170] Z. Xiao, H. Hiramatsu, S. Ueda, Y. Toda, F.-Y. Ran, J. Guo, H. Lei, S. Matsuishi, H. Hosono, and T. Kamiya, Narrow bandgap in β-$BaZn_2As_2$ and its chemical origins, Journal of the American Chemical Society **136**, 14959 (2014).

[171] H. Xin and X. Qin, Electrical and thermoelectric properties of nanocrystal substitutional semiconductor alloys $Mg_3(Bi_xSb_{1-x})_2$ prepared by mechanical alloying, Journal of Physics D: Applied Physics **39**, 5331 (2006).

[172] C.-S. Yoon, F. Medina, L. Martinez, T.-Y. Park, M.-S. Jin, and W.-T. Kim, Blue photoluminescence of α-Ga_2S_3 and α-Ga_2S_3:Fe^{2+} single crystals, Applied physics letters **83**, 1947 (2003).

[173] M. Yoshida, T. Katsumata, and Y. Inaguma, High-pressure synthesis, crystal and electronic structures, and transport properties of a novel perovskite $HgSnO_3$, Inorganic Chemistry **47**, 6296 (2008).

[174] J. ZHANG, L. SHAO, Y. FU, and E. XIE, Cu_2ZnSnS_4 thin films prepared by sulfurization of ion beam sputtered precursor and their electrical and optical properties, Rare Metals **25**, 315 (2006).

[175] S. Zhang, M. Yoshikawa, K. Inumaru, and S. Yamanaka, Topochemical cross-linking of the $[Hf_2N_2]$ layers with sulfur in α-HfNBr, Inorganic Chemistry **52**, 10571 (2013).

[176] N. Zhou, G. Chen, H. Zhang, and C. Zhou, Computational and experimental studies of optical absorption properties of perovskite-layered $SrO(SrTiO_3)_n$ ($n = 1, 2, \cdots, \infty$), Journal of alloys and compounds **477**, L17 (2009).

[177] D. Zimmer, J. Ruiz-Fuertes, L. Bayarjargal, E. Haussühl, B. Winkler, J. Zhang, C. Jin, V. Milman, E. Alig, and L. Fink, Phase transition of tetragonal copper sulfide Cu_2S at low temperatures, Physical Review B **96**, 054108 (2017).

FIGURE LEGENDS

Figure 1. Bandgap variation across the κ–c_{1x} space. Color maps show the predicted electronic bandgap E_g as a function of κ and c_{1x} for: (a) carbon diamond, (b) silicon, and (c) germanium. For carbon, the white line encloses the region with the maximum bandgap. For silicon and germanium the white line represents all the solutions that achieve the experimental bandgap. The color bar reports E_g as a percentage of the experimental value. Warmer (cooler) colors denote larger (smaller) bandgaps.

Figure 2. Lattice parameter across the κ–c_{1x} space. Color maps show the relaxed cubic lattice parameter (a in Å) as a function of κ and c_{1x} for: (a) carbon diamond, (b) silicon, and (c) germanium. The white curve represents the solutions that achieve the experimental lattice parameters in all cases. The color bar reports a as a percentage of the experimental value. Warmer (cooler) colors denote larger (smaller) bandgaps.

Figure 3. Variation of h_x^α as a function of κ. Curves show the behavior of h_x^1 (blue) and h_x^0 (green) as a function of κ for fixed s=1. Default κ is shown as a dashed line. The value of h_x^α lies between h_x^1 and h_x^0 and depends on α.

Figure 4. Dependence of the interpolation factor $f_x(\alpha)$ on c_{1x}. Curves show f_x versus α for different values of c_{1x}: 0.1 (red), 0.2 (blue), and 0.667 (green; SCAN default).

Figure 5. Band structures with different exchange–correlation functionals. (a) Carbon (diamond). (b) GaAs. Curves colors denote functionals: PBE (blue), SCAN (green), and SD-SCAN (red). The hatched region visually indicates the experimental fundamental bandgap. (Image generated with PyProcar[63, 64].)

Figure 6. Charge density with different exchange–correlation functionals for carbon diamond. Charge density distribution for (a) LDA, (b) PBE, (c) SCAN, and (d) SD-SCAN. (Images generated with VESTA at an isosurface level of 0.251357 [65].)

Figure 7. Dielectric function with different exchange-correlation functionals. Real (top) and imaginary (bottom) part of the dielectric function of silicon. Spectra computed with PBE (blue), SCAN (green), and SD-SCAN (red). Experimental data from Ref. [71] is shown for comparison (black dashed line).

TABLE LEGENDS

Table 1. Performance of the SD-SCAN exchange–correlation functional. Bandgap values (eV) and lattice parameters (Å) of representative solids obtained using different exchange–correlation functionals. Materials are grouped by crystal system (CS): diamond-like (diam), face-centered cubic (fcc), rocksalt (rs), zincblende (zb), and hexagonal (hex). For cubic structures, only the a-lattice parameter is reported, while for hexagonal structures both a- and c-lattice parameters are provided. The optimized parameters (κ, c_{1x}, d_x, and c_{1c}) correspond to the values used in the SD-SCAN functional for each material. The last row reports the average mean absolute error (MAE), excluding noble gases.

Table 2. Optical dielectric constant predictions using different exchange–correlation functionals. Optical dielectric constants, $\epsilon(\infty)$, of representative solids obtained using different exchange–correlation functionals. Experimental values are taken from Ref. [1]. Mean error and mean absolute error are reported for comparison. Average values exclude materials classified as metals in any case.

Table 3. Bandgap predictions using machine learning and the SCAN-0.2 functional. Mean absolute error (standard deviation) using PBE, SCAN, SD-SCAN, SCAN-0.2, and ML-SCAN in predicting the bandgap (eV) of various semiconductors and insulators classified by crystal system (CS). ML-SCAN values correspond to the leave-one-out cross-validation (LOOCV) out-of-sample accuracy of the multiple linear regression (MLR) algorithm.

Table 4. Bandgap prediction for cubic systems. Mean absolute error (standard deviation) using PBE, SCAN, SD-SCAN, SCAN-0.2, and ML-SCAN in predicting the bandgap (eV) of various cubic semiconductors and insulators subclassified by crystal system (CS). ML-SCAN values correspond to the leave-one-out cross-validation (LOOCV) out-of-sample accuracy of the multiple linear regression (MLR) algorithm.